Square-triangle tilings: an infinite playground for soft matter

Marianne Impéror-Clerc, Anuradha Jagannathan, Pavel Kalugin, Jean-François Sadoc

Soft Matter

ARTICLE TYPE

Cite this: DOI: 00.0000/xxxxxxxxxx

Square-triangle tilings : An infinite playground for soft matter†

Marianne Impéror-Clerc,*[a] Anuradha Jagannathan,[a] Pavel Kalugin,[a] and Jean-François Sadoc[a]

Received Date
Accepted Date

DOI: 00.0000/xxxxxxxxxx

Regular square and triangle, two very simple geometrical figures, can be used to construct a fascinating variety of tilings which cover the 2D plane without any overlaps or holes. Such tilings are observed in many soft matter systems. Here we present a way to describe all possible globally uniform square-triangle phases using a three dimensional composition space. This approach takes into account both the overall composition and the orientations of the two kinds of tiles. The geometrical properties of special phases encountered in soft matter systems are described: the Archimedean Σ and H phases, the striped phases and the 12-fold maximally symmetric phases. We show how this very rich behavior with either periodic or aperiodic phases appears here as a consequence of the inherent incommensurability between the areas of the two tiles related by the ratio $\sqrt{3}/4$. Geometrical constraints on boundary lines and junction points between domains of different compositions are given, a situation likely to be encountered in experimental and numerical studies. Future developments are suggested like considering the effect on phase behavior of possible symmetry breaking.

1 Introduction

There is a renewal of interest in the geometrical properties of square-triangle tilings as they are observed in many experimental systems at the nanoscale such as liquid crystals,[1–3] copolymers,[4] mesoporous materials,[5–7] nanoparticles super-lattices,[8] photonic materials,[9–11] along with numerical simulations studies[12–15]. In all these soft matter systems, some phases can be described by an underlying square-triangle tiling as illustrated in Figure 1 by the example of a dodecagonal mesoporous material. Such square-triangle phases are encountered either in pure bi-dimensional systems like in the numerical simulations of binary mixtures of hard disks[16–18] or in self-assembled three dimensional phases formed by liquid-crystals, copolymers, surfactants. In the case of a three dimensional phase, the structure is always a periodic stack of two dimensional layers containing the same square-triangle tiling. Such three dimensional stacks of 2D layers have been discussed elsewhere.[4,19] It is then sufficient to consider only bi-dimensional square-triangle phases.

When quasicrystals were discovered in metallic alloys during the 80's, square-triangle tilings became popular models for phases with 12-fold symmetry. Square-triangle tilings had been just introduced in statistical mechanics as models of 2D amorphous lattices.[20] Within a few years in the middle of the 90's, the analytical calculation of the entropy of configuration of square-triangle tilings could be solved thanks to advanced statistical mechanics Bethe-Ansatz methods.[21–24] The proposed models for 12-fold quasicrystals were either deterministic (with a well-defined rule for their construction) or random, and, for the later case, it has been argued that the latter should be favored on entropic

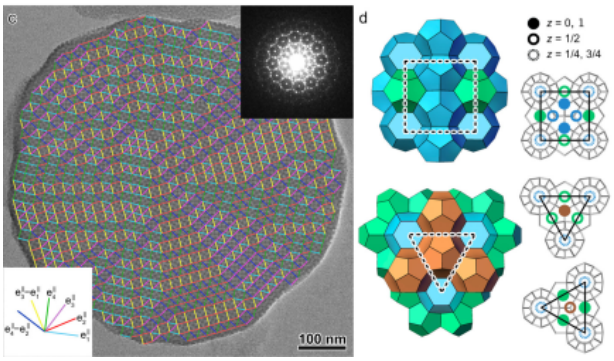

Fig. 1 A dodecagonal mesoporous material (Adapted from reference[7]). The high resolution transmission electron microscopy of a single mesoporous particle is analyzed with a finite patch of square and triangle tiles with different orientations (see Figs. 2 and 3 later on). In the inset, the electron diffraction pattern shows a 12-fold symmetry. The two tiles correspond to the two building units of the mesoporous material, a cube and a triangular prism that are shown one the right. Each building unit contains several cavities depicted by their polyhedral Voronoi cells in different colors.

[a] LPS, Laboratoire de Physique des Solides, CNRS, Université Paris-Saclay, Orsay, France; E-mail: marianne.imperor@universite-paris-saclay.fr

† Electronic Supplementary Information (ESI) available: [details of any supplementary information available should be included here]. See DOI: 10.1039/cXsm00000x/

grounds.[21,22] However, the relative merits of deterministic versus random tilings models are still a matter of debate.[25]

In addition to the 12-fold symmetric phases that attract much attention, soft matter systems can display a large variety of other square-triangle phases. There is a need now to consider square-triangle phases in a more global way, with no restriction to the case of 12-fold symmetry, in order to understand their very rich phase behavior. Given a system with a fixed composition (in terms of the relative amount of triangles and squares), one may ask what kind of phases could be observed. Out-of-equilibrium states may be reached and the entropy of configuration may be not the only factor to be taken into account.

The outline of the paper is as follows. After introducing square-triangle tilings, we explain the notion of global uniformity for infinite tilings which is necessary to define their composition (section 2). We conclude that only three independent parameters are needed to specify the composition. A three-dimensional "composition space" is built accordingly and is systematically explored (section 3). This approach allows to take into account both the overall composition and the distribution in orientation of the two kinds of tiles. The link between composition and lifting in 4D space is made (section 4) and special phases encountered in soft matter systems are described in this context (section 5): the Archimedean Σ and H phases, the striped phases and the 12-fold maximally symmetric phases. Geometrical constraints on boundary lines and junction points between domains of different compositions are given (section 6), a situation likely to be encountered in experimental and numerical studies. Finally, the geometrical features of square-triangle phases are summarized and predictions about their phase behavior are made (section 7). In addition to the main text, the interested reader will find in the †file introductions about geometrical concepts (lift in 4D, inflation construction, diffraction) along with many specific mathematical derivations.

2 Tiles, area fractions and global uniformity

2.1 Square-triangle tilings

Squares and triangles can be combined edge-to-edge in many ways to cover the 2D plane without any overlaps or holes. Even if the two tiles, regular squares and triangles, are simple geometrical objects, there is a fascinating variety in the different patterns/patches they can form to tile the 2D plane. Indeed, combining regular squares and triangles introduces naturally some 'incommensurability' in the system coming from the irrational ratio $\sqrt{3}/4$ between the areas of the two tiles. This notion of incommensurability will be elaborated further on, particularly in section 5.3 about the striped phases that are made of 1D stacks of infinite stripes of squares and triangles.

Let us start by considering a finite patch of square-triangle tilings like the one depicted on Figure 2. We denote the number of squares and triangles in the patch $\mathscr{P}$ by $N_s(\mathscr{P})$ and $N_t(\mathscr{P})$ respectively. We use the notation $|\mathscr{P}|$ for the area of the patch $\mathscr{P}$ and $|\partial\mathscr{P}|$ for the total length of its boundary $\partial\mathscr{P}$.

Since the tiles are either regular squares or equilateral triangles, of the same edge size a, the constraint of covering the entire plane by packing tiles tightly together edge-to-edge implies that all tile edges have only six possible orientations, labelled from $\mathbf{e}_1$ to $\mathbf{e}_6$, with relative angles all multiple of $\pi/6$:

$$\mathbf{e}_i = a \begin{pmatrix} \cos\frac{\pi(i-1)}{6} \\ \sin\frac{\pi(i-1)}{6} \end{pmatrix}. \quad (1)$$

This geometrical property explains why long range orientational order is always present in such tilings. The associated symmetry may be 4-fold, 6-fold or 12-fold, as will be explained later on.

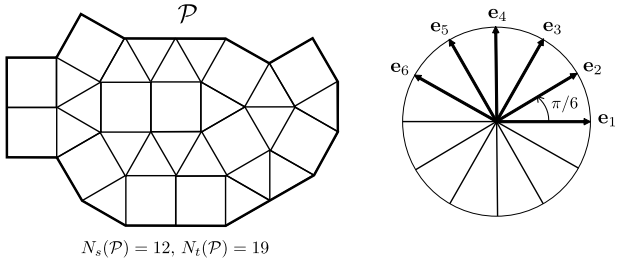

Fig. 2 A finite patch $\mathscr{P}$ of a square-triangle tiling with 12 squares and 19 triangles. All edges have the same length a and have six possible orientations labelled from $\mathbf{e}_1$ to $\mathbf{e}_6$.

Since there are only six possible orientations for edges, there are a finite number of possible orientations for the tiles, as shown in Figure 3. Square tiles can have three different orientations, noted S_1, S_2 and S_3. For example, edges of a square tile with orientation S_1 are along $\mathbf{e}_1$ and $\mathbf{e}_4$. Triangles can have four different orientations, called here T_1, T_2, T_3 and T_4. In all, seven different tiles must be considered, if one takes into account their orientations. They are drawn in Figure 3. Edges of the T_1 and T_3 triangular tiles are along $\mathbf{e}_1$ and $\mathbf{e}_3$, when the edges of T_2 and T_4 tiles are along $\mathbf{e}_2$ and $\mathbf{e}_4$. Edges have been colored red or blue in order to distinguish the T_1 and T_3 triangles (in blue) from the T_2 and T_4 ones (in red). The same color code is used in the next Figures to distinguish triangle's orientations. Moreover, following[17], it is convenient to add dotted extra lines on the tiles or 'decoration' lines. These extra lines serve to indicate the orientation of the tiles within a structure. Note that we are drawing the tilings in the different figures with the direction of $\mathbf{e}_1$ always along the horizontal direction.

In a similar manner, the tiles can combine in a finite number of four different vertices, noted 4^4, 3^6, 3^2434 and 3^34^2 (see Figure 3). The notation corresponds to the tiles sequence around a vertice. If one takes into account the orientation of the tiles, each type of vertices may have different orientations. The 4^4 vertice can have three different orientations of the tiles, corresponding to the S_1, S_2 and S_3 tiles. The 3^6 vertice has two orientations. The two other types of vertices, 3^2434 and 3^34^2, have twelve different possible orientations, leading to a total number of 29 different vertices taking into account their orientation.

2.2 Composition of infinite tilings

Here we consider infinite tilings of the plane. This is based on the assumption that properties of a sufficiently large experimental system can be described by the properties on an infinite tiling.

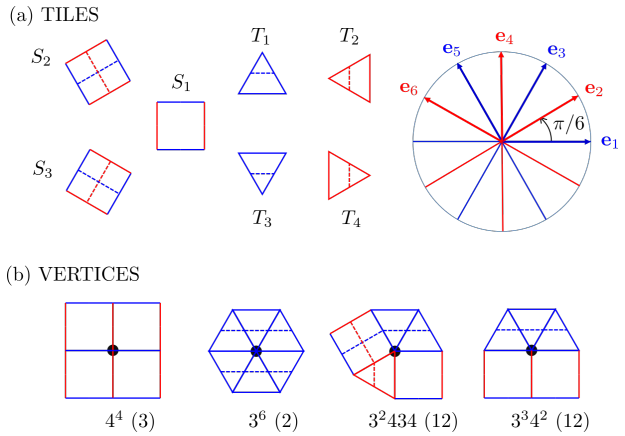

Fig. 3 (a) The seven tiles when taking orientation into account. Squares can have three different orientations (labelled S_1, S_2 and S_3) when triangles can have four (T_1, T_2, T_3 and T_4). Edges in T_1 and T_3 (respectively T_2 and T_4) triangles are depicted in blue (red) color. The same color code is applied for the square tiles (S_1, S_2, S_3), which all exhibit two blue and two red edges. (b) The four types of vertices. The number of possible orientations for each of them are respectively : three for 4^4 vertice, two for 3^6 vertice and 12 for both the 3^2434 and 3^34^2 vertices. The dashed lines inside tiles are 'decoration' lines, as introduced in [17]. By convention the direction of $\mathbf{e}_1$ is along the horizontal axis in the Figures.

Border effects are thus not present but can be taken into account later after we have defined properly the composition of an infinite tiling.

When referring to area fraction of tiles of a given type in such an infinite tiling, we shall implicitly assume that it can be obtained as a limit of the area fraction for its finite patches, as their size goes to infinity. To exclude the influence of boundary effects, we shall consider only the situation when the area of the patch $\mathscr{P}$ scales as the square of its perimeter, that is there exists a positive constant c such that

$$|\mathscr{P}| > c|\partial\mathscr{P}|^2 \tag{2}$$

It should be emphasized that for a given tiling of the entire plane this limit does not necessarily exist. Consider for instance the situation when half of the plane is covered by squares and the other half by triangles. In this case one can find two sequences of growing finite roundly-shaped patches, each contained in the respective half-plane, and thus always having different compositions (see later section 6).

We shall consider only the infinite tilings for which the limit of the area fraction is well-defined. We shall call this assumption *the global uniformity condition* (see Figure 4). Periodic tilings provide an obvious example of this condition, since in them the area fractions of tiles of a given type are fixed by their numbers in any unit cell patch. The precise characterization of generic globally uniform tilings -based on lifting maps- is given in Section 4.

We shall denote the area fraction occupied by squares and triangles in a patch $\mathscr{P}$ by $\sigma(\mathscr{P})$ and $\tau(\mathscr{P})$:

$$\begin{aligned}\sigma(\mathscr{P}) &= a^2 N_s(\mathscr{P})/|\mathscr{P}| \\ \tau(\mathscr{P}) &= \frac{\sqrt{3}}{4}a^2 N_t(\mathscr{P})/|\mathscr{P}|.\end{aligned}$$

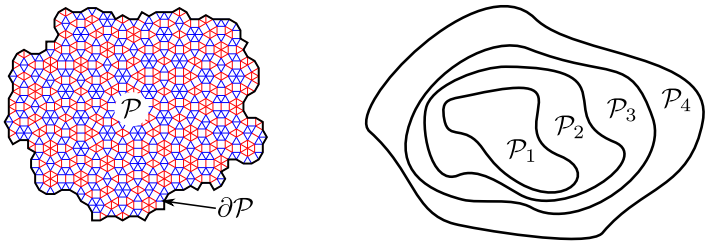

Fig. 4 An illustration to the global uniformity condition. In the sequence of finite patches $\mathscr{P}_i$, the area $|\mathscr{P}|$ of the patch $\mathscr{P}$ scales as a square of its perimeter $|\partial\mathscr{P}|$. More specifically, there exists a constant $c > 0$ such that $|\mathscr{P}_i| > c|\partial\mathscr{P}_i|^2$ for all i. The infinite tiling is called globally uniform if for any such sequence of patches the area fraction of any given tile species converges to the same limit.

To distinguish the number of tiles of a given orientation in a patch $\mathscr{P}$, we shall use a numerical index, for instance, $N_{s1}(\mathscr{P})$ will stand for the number of squares S_1 and $N_{t2}(\mathscr{P})$ for the number of triangles T_2, with the obvious identities

$$\begin{aligned}N_s(\mathscr{P}) &= N_{s1}(\mathscr{P})+N_{s2}(\mathscr{P})+N_{s3}(\mathscr{P}) \\ N_t(\mathscr{P}) &= N_{t1}(\mathscr{P})+N_{t2}(\mathscr{P})+N_{t3}(\mathscr{P})+N_{t4}(\mathscr{P}).\end{aligned}$$

Similarly, we shall use the numerical index to denote the area fraction occupied by tiles of a given orientation, for instance $\tau_1(\mathscr{P})$ will stand for the area fraction of triangles T_1 in the patch $\mathscr{P}$.

The global uniformity condition requires that for any sequence of growing patches like that shown on Figure 4 the area fractions of each tile species have a well-defined limit, which we will denote for brevity by the same symbol, omitting the name of the patch, for instance

$$\lim_{i\to\infty}\tau_1(\mathscr{P}_i) = \tau_1. \tag{3}$$

In addition to the obvious constraint

$$\sigma + \tau = 1 \tag{4}$$

we also have the identities $\tau_1 = \tau_3$ and $\tau_2 = \tau_4$ (see e.g.[17]). This statement can be understood from the following simple argument. Consider a triangle T_1 in a patch $\mathscr{P}$ and draw a ray from its center perpendicular to the edge $\mathbf{e}_1$. There are only two possibilities: either this ray hits a center of a triangle T_3 (maybe after crossing several squares S_1), in which case we shall say that this triangle T_3 is coupled with the considered triangle T_1, or it will cross the boundary of $\mathscr{P}$ at the center of a segment parallel to $\mathbf{e}_1$. Thus, the number of uncoupled triangles scales as the boundary of $\mathscr{P}$:

$$N_{t1}(\mathscr{P}) - N_{t3}(\mathscr{P}) \sim |\partial\mathscr{P}|$$

and the identity $\tau_1 = \tau_3$ follows from the assumption $|\partial\mathscr{P}|/|\mathscr{P}| \to 0$. We can therefore reduce the number of independent area fractions by two. With the notations $\tau_{13} = \tau_1 + \tau_3$ and $\tau_{24} = \tau_2 + \tau_4$, equation 4 reads (as $\sigma = \sigma_1 + \sigma_2 + \sigma_3$)

$$\sigma_1 + \sigma_2 + \sigma_3 + \tau_{13} + \tau_{24} = 1. \tag{5}$$

The five area fractions σ_1, σ_2, σ_3, τ_{13} and τ_{24} are also linked by

another relation, which reads as follows:

$$\sigma_1\sigma_2 + \sigma_2\sigma_3 + \sigma_3\sigma_1 = 4\tau_{13}\tau_{24}/3 \tag{6}$$

This second relation is much less trivial than equation 5 as it involves products of the area fractions. We provide a demonstration of this relation later on in section 4 using lifting maps. To our knowledge, this relation was first introduced by B. Nienhuis[24] and we term equation 6 the "Nienhuis relation".

In sum, the five area fractions satisfy two relations, the coverage relation (equation 5) and the Nienhuis relation (equation 6). **This implies that one requires only $3 = 5 - 2$ independent parameters to specify any given composition**. Consequently, we can built a three dimensional composition space, and this is described in the next section.

3 3D composition space

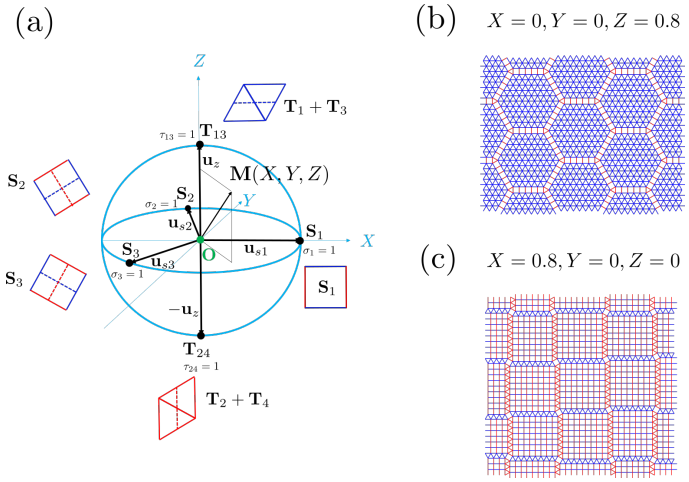

Fig. 5 Barycentric representation of the three dimensional composition space. (a) The unit sphere is shown in light blue with the five unit vectors. A particular composition $(X,Y,Z,)$ correspond to a composition point $\mathbf{M}(X,Y,Z)$ (see Eq.8a). The five points $\mathbf{S}_1$, $\mathbf{S}_2$, $\mathbf{S}_3$, $\mathbf{T}_{13}$ and $\mathbf{T}_{24}$ correspond to the five "pure" phases consisting only of squares or triangles of a *single* family, as illustrated in the small patches surrounding the unit sphere. Two examples of phases are given for (b) a composition point along the OZ direction at $(0,0,0.8)$ showing a 3-fold symmetry and (c) along the OX (c) at $(0.8,0,0)$ showing a 4-fold symmetry. Both phases are composed either of a majority of T1/T3 tiles in (b) or S1 tiles in (c).

3.1 Barycentric representation

In order to represent the three dimensional composition space, we use the barycentric representation due to Kalugin,[23] that provides a convenient way to represent the set of five area fraction variables $\{\sigma_1, \sigma_2, \sigma_3, \tau_{13}, \tau_{24}\}$. Such representations are commonly used for ternary systems, where there are three variables which must sum to a constant. This scheme can be extended to describe our quinary system with five unit vectors introduced in the following way. For each of the three σ variables, three units vectors form a triad in the plane XY:

$$\begin{aligned}
\mathbf{u}_{s1} &= \mathbf{OS}_1 = \mathbf{u}_x \\
\mathbf{u}_{s2} &= \mathbf{OS}_2 = -(1/2)\mathbf{u}_x + (\sqrt{3}/2)\mathbf{u}_y \\
\mathbf{u}_{s3} &= \mathbf{OS}_3 = -(1/2)\mathbf{u}_x - (\sqrt{3}/2)\mathbf{u}_y
\end{aligned} \tag{7}$$

In addition, we introduce two unit vectors for the τ_{13} and τ_{24} variables pointing upwards (downwards) along the z-axis. In terms of these unit vectors, shown in Figure 5, any given tiling composition can be represented by a point M with three Cartesian coordinates (X,Y,Z) given by

$$\mathbf{OM} = X\mathbf{u}_x + Y\mathbf{u}_y + Z\mathbf{u}_z = \sigma_1\mathbf{u}_{s1} + \sigma_2\mathbf{u}_{s2} + \sigma_3\mathbf{u}_{s3} + \tau_{13}\mathbf{u}_z + \tau_{24}(-\mathbf{u}_z) \tag{8a}$$

$$X = \left(\sigma_1 - \frac{\sigma_2+\sigma_3}{2}\right); Y = \frac{\sqrt{3}}{2}(\sigma_2 - \sigma_3); Z = (\tau_{13} - \tau_{24}) \tag{8b}$$

In Figure 5a, the five points $\mathbf{S}_1$, $\mathbf{S}_2$, $\mathbf{S}_3$, $\mathbf{T}_{13}$ and $\mathbf{T}_{24}$ play a special role as they correspond to the five possible "pure" phases, made of the regular tilings of squares and triangles. Because orientation is taken into account, they are three "pure" phases with squares (S_1, S_2 and S_3 phases) and two with triangles (T_{13} and T_{24} phases). Two examples of phases at two composition points located along the OZ (Fig. 5b) and OX (Fig. 5c) directions are also given. These phases reflect the symmetry in the orientation of the tiles.

For $X = Y = Z = 0$, when the point $\mathbf{M}$ coincides with the point $\mathbf{O}$, all the area fractions have fixed values :

$$\begin{aligned}
\sigma_1 = \sigma_2 = \sigma_3 &= \frac{\sigma}{3} = \frac{1}{6} \\
\tau_{13} = \tau_{24} &= \frac{\tau}{2} = \frac{1}{4}
\end{aligned} \tag{9}$$

Indeed, all the allowed orientations of squares and triangles are present *with equal area fractions* at the point O. We term *"maximally symmetric"* the corresponding tilings, to signify that the distribution of tile orientations is maximally symmetric at point O. The specific properties of such tilings are discussed later on in section 5.4.

Reversely (by combining Eqs.5, 6 and Eqs in 8b), for any composition point, the five area fractions can be expressed in terms of its coordinates X,Y,Z :

$$\begin{aligned}
\sigma_1 = \frac{2X+1-\tau}{3}; \sigma_2 = \frac{1-X-\tau}{3} + \frac{Y}{\sqrt{3}}; \sigma_3 = \frac{1-X-\tau}{3} - \frac{Y}{\sqrt{3}} \\
\tau_{13} = \frac{1}{2}(\tau+Z); \tau_{24} = \frac{1}{2}(\tau-Z)
\end{aligned} \tag{10}$$

Finally, the overall composition, defined by the τ parameter at any composition point X,Y,Z reads:

$$\tau = \frac{1}{2}\left(1+Z^2-X^2-Y^2\right) \iff \tau-\sigma = Z^2-X^2-Y^2 \qquad (11)$$

This relation that contains quadratic terms in X, Y and Z comes from the Nienhuis relation (Eq. 6) which is demonstrated later on in section 4 using lifting maps in 4D space.

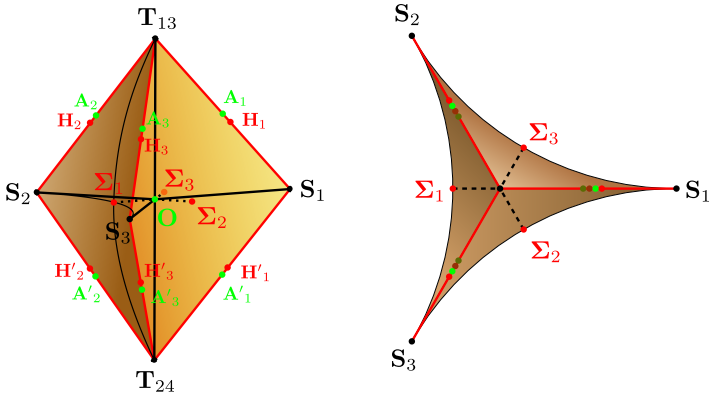

Fig. 6 Side and top views of the allowed sub-volume $\mathscr{V}$ in the 3D composition space. The "pure phases" correspond to the five apexes of the sub-volume $\mathscr{V}$, points $\mathbf{S}_1$, $\mathbf{S}_2$, $\mathbf{S}_3$, $\mathbf{T}_{13}$ and $\mathbf{T}_{24}$ (see Figure 5). The red lines joining apexes correspond to striped phases (see section 5.3). Special points corresponding to $\tau = 1/2$ (green) and $\tau = 2\sqrt{3}-3 \simeq 0.464$ (red) are also indicated (see also Figure 7 and Table 1).

3.2 Sub-volume in the 3D composition space

Since all five area fractions must lie between 0 and 1, some regions of the unit sphere are unphysical, i.e. do not correspond to any composition. Using the relations in Eqs.10 one finds that the allowed volume, $\mathscr{V}$, is bounded by the three surfaces given by the equations $\sigma_1 = 0$, $\sigma_2 = 0$ and $\sigma_3 = 0$. The volume $\mathscr{V}$, whose side and top views are shown in Figure 6, has a three-fold symmetry with respect to rotation about the z axis and a mirror symmetry with respect to the XY plane. As introduced later on in section 4, in the tiling plane P, a rotation by $\pi/6$ corresponds to a cyclic permutation of the points $\mathbf{S}_1$, $\mathbf{S}_2$ and $\mathbf{S}_3$ and a transposition of the points $\mathbf{T}_{13}$ and $\mathbf{T}_{24}$. It is thus sufficient to describe the tilings in one-third of $\mathscr{V}$, as all the others can be deduced by symmetry. Thus, for example, one can choose to consider the region subtended by the surface $\sigma_1 = 0$, which reads :

$$Z^2 = X^2 + Y^2 + 4X + 1 \qquad (12)$$

The intersections of this surface with the XY plane (a circle) and the XZ plane (a hyperbola) are shown as thin dark lines in Figure 6. These two lines intersect at the special point $\mathbf{\Sigma}_1$ located at the intersection of the surface $\sigma_1 = 0$ with the X axis at $X = \sqrt{3}-2 \simeq -0.268$. By symmetry, there are two other equivalent points, labeled $\mathbf{\Sigma}_2$ and $\mathbf{\Sigma}_3$. The corresponding tilings are discussed in more detail in section 5.1.

We turn to the six straight lines shown in red in Fig. 6, which link each of the points T_{ij} with the S_i. These lines are associated with striped phases: 1D stacks of stripes of squares of a single orientation followed by stripes of triangles of a given family. These structures will be detailed in section 5.3.

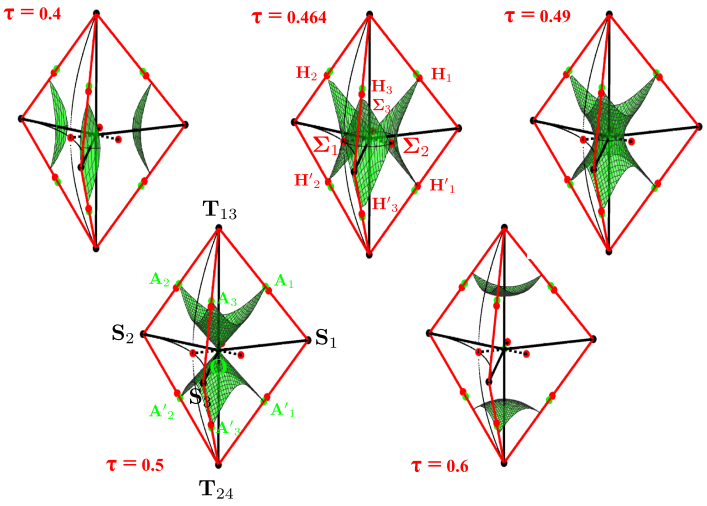

Fig. 7 τ-surfaces in the three dimensional composition space. The τ-surfaces are hyperboloids with three sheets for $\tau < 2\sqrt{3}-3 \simeq 0.464$, a single sheet for $2\sqrt{3}-3 < \tau < 1/2$, and two sheets for $1/2 < \tau < 1$. The special points in green, $\mathbf{O}$, $\mathbf{A}_1$, $\mathbf{A}_2$,... for $\tau = 0.5$, and the special points in red $\mathbf{\Sigma}_1$, $\mathbf{\Sigma}_2$, $\mathbf{\Sigma}_3$, $\mathbf{H}_1$, $\mathbf{H}_2$,...for $\tau = 0.464$ are the same as in Fig.6.

3.3 Surfaces for fixed values of the area fraction τ

Here we discuss the different τ-surfaces corresponding to a fixed value of the total area fraction of triangles, τ. Using equation (11) which relates the value of τ to the coordinates X,Y,Z, it can be shown that these τ-surfaces are hyperboloids of one or two sheets as shown in Figure 7. We now list the different types of τ-surfaces as τ is decreased from 1 (corresponding to a pure triangular lattice):

- $\frac{1}{2} \le \tau \le 1$: the τ-surfaces are composed of two disconnected sheets: one for $Z > 0$ and the other for $Z < 0$. The sheets are symmetric with respect to reflection about the XY plane: Since $Z = \tau_{13} - \tau_{24}$ (see Eqs. 10), changing the sign of Z corresponds to interchanging the roles of the triangles T_1 and T_3 and the triangles T_2 and T_4. For $\tau = 1$, the two sheets shrink into the two points $\mathbf{T}_{13}$ and $\mathbf{T}_{24}$, corresponding to the two regular triangular tilings.

- $\tau = \frac{1}{2}$ is a critical value of τ, for which the τ-surface is a conical surface of apex $\mathbf{O}$ (see Figure 7). For this value of τ, the ratio of squares and triangles is an irrational number: $N_t/N_s = 4/\sqrt{3}$. Periodic tilings corresponding to this value of τ are therefore ruled out but aperiodic structures can exist. The intersections of the conical surface for $\tau = 1/2$ with the boundary of the volume $\mathscr{V}$ give the six special points $\mathbf{A}_1$, $\mathbf{A}_2$,... shown in green in Figs. 6 and 7. These points correspond to 1D aperiodic 'striped phases' which are discussed later in section 5.3. At point O, all tilings are maximally symmetric with respect to the tiles orientation distribution and this give rise to 2D aperiodic ordered phases also known as quasicrystals (see section 5.4).

- $2\sqrt{3}-3 \le \tau \le \frac{1}{2}$: The τ-surface is composed of a single sheet

(see Figure 7). The critical value $\tau = 2\sqrt{3}-3 \simeq 0.464$ corresponds to all compositions for which the number of triangles is twice the number of squares, such that $N_t/N_s = 2$. For this value of τ, periodic tilings can be encountered such as the Archimedean Σ and H phases discussed in section 5.1 and 5.2.

- $0 \leq \tau \leq 2\sqrt{3}-3$ In this range of values a τ-surface is composed of three disconnected sheets (see Figure 7). Each of these sheets shrinks to a point as $\tau \to 0$, giving the three regular square tilings ('pure" phases corresponding to the points $\mathbf{S}_1$, $\mathbf{S}_2$ and $\mathbf{S}_3$) in this limit.

4 Composition and lift in 4D space

A general and powerful approach is to associate a two-dimensional tiling (see Section 2.2) with a subset of a periodic arrangement in a space of higher dimension, called a superspace, containing the tiling plane P as a subspace.[25,26] The original tiling then arises as a projection of this subset, which is commonly referred to as a "lifted" tiling.[26,27] The advantage of such lift construction is that a unique periodic lattice in the superspace contains all possible subsets. A more delicate associated question is to define how to select a subset in the periodic lattice. For square-triangle tilings, a standard lift construction is already known[21] and is described in details in the †ESI file (part A). The superspace has four dimensions and is noted $P \oplus P_\perp$, where $P_\perp$ is a 2D-plane orthogonal to P. The 4D lattice is the direct sum of two regular triangular lattices (see A.2 in †file and Fig. 19).

In this section, we first explain the relationship between the 3D composition space and the lifting scheme by introducing the notions of lifting maps, hyperslopes and pure phases (section 4.1). We then give a precise characterization of the global uniformity and a demonstration of the Nienhuis relation (section 4.2).

4.1 Lifting maps, hyperslopes and "pure phases"

The lift of a square-triangle tiling can be conveniently described in terms of the so-called "lifting map" $\varphi : P \to P_\perp$ defined on the vertices of the tiling as $\varphi(\mathbf{v}) = \mathbf{v}_\perp$ and continued to the interior of the tiles and their edges by linear interpolation.[21] $\mathbf{v}$ and $\mathbf{v}_\perp$ are the components of a 4D-vertex respectively in P and $P_\perp$ (†ESI file part A.2). Let us first illustrate this idea on the simplest case of the "pure" phases (points $\mathbf{S}_1$, $\mathbf{S}_2$, $\mathbf{S}_3$, $\mathbf{T}_{13}$, $\mathbf{T}_{24}$ in the 3D composition space, see Figure 6), where the plane P is entirely tiled either by triangles or squares. Here the term of "pure" phase is chosen by analogy with a pure component in the phase diagram of a mixture. For instance, in the pure phase corresponding to the composition point $\mathbf{T}_{13}$, the pure phase is the regular triangular lattice of tiles T_1 and T_3 and the coordinates of all vertices has the form $\mathbf{v} = n_1\mathbf{e}_1 + n_3\mathbf{e}_3$. Simultaneously in $P_\perp$, the associated vertices are $\mathbf{v}_\perp = n_1\mathbf{e}_{1_\perp} + n_3\mathbf{e}_{3_\perp}$ and form a similar triangular lattice. The same construction is possible for all other pure phases and their lifting maps φ are all a linear function on the set of vertices of the tiling (and thus on the entire plane P):

$$\mathbf{v}_\perp = \varphi(\mathbf{v}) = B^\Phi \cdot \mathbf{v}, \tag{13}$$

where B^Φ is a real 2×2 matrix corresponding to the pure phase Φ among the five matrices B^{T13}, B^{T24}, B^{S1}, B^{S2} and B^{S3} (see Table 2). Remarkably, these matrices are always symmetric. It should be emphasized that this is not an intrinsic property of the lifting scheme, but a peculiarity of the square-triangle tiling. In particular, since adding 30-degrees rhombi to the tiling does not modify the set of allowed directions of tiles edges, such tilings can also be lifted following the same recipe.[28,29] However, although the lifting map for the pure phase of rhombi is also linear, the corresponding matrix is non-symmetric.

As follows from the above, the lifted tiling for the pure phase composed by triangles T_1 and T_3 is a triangular lattice in the 2D-plane $P_{T_{13}}$. By applying the similar reasoning to other pure phases, one can also construct the 2D-planes $P_{T_{24}}$, P_{S_1}, P_{S_2} and P_{S_3}. In each case, the matrix B^Φ corresponds to the "hyperslope" of the corresponding plane with respect to P (†ESI file part A.2).

We can now consider the more general case where the tiling is a mixture of different types of tiles. In this case φ is a piecewise-affine function on P. However, this function has a constant slope on the interior of each tile:

$$\frac{\partial \varphi_\alpha(\mathbf{x})}{\partial x^\beta} = B^\Phi_{\alpha\beta}. \tag{14}$$

Here x^β are the components of $\mathbf{x}$ in the standard orthonormal basis of P, $\varphi_\alpha(\mathbf{x})$ are the components of $\varphi(\mathbf{x})$ in the respective orthonormal basis of $P_\perp$ and the matrix B^Φ corresponds to the pure phase Φ containing the considered type of tiles. Since B^Φ is symmetric (as it is the case for all pure phases), the function φ has an important "irrotational property", holding in the interior of each tile:[21]

$$\frac{\partial \varphi_1(\mathbf{x})}{\partial x^2} - \frac{\partial \varphi_2(\mathbf{x})}{\partial x^1} = B^\Phi_{12} - B^\Phi_{21} = 0. \tag{15}$$

4.2 Global uniformity and Nienhuis relation

We can now give an exact characterization of the class of *globally uniform* tilings, that is those with a well-defined composition, namely such that for every sequence of finite patches with asymptotically negligible boundary, the composition of the patches converges to the same limit:

Proposition 1 *The square-triangle tiling is globally uniform if and only if its lifting map φ is asymptotically linear, that is there exists a linear operator $B : P \to P_\perp$ such that*

$$\varphi(\mathbf{x}) = B \cdot \mathbf{x} + o(\|\mathbf{x}\|), \tag{16}$$

where $o(\|\mathbf{x}\|)$ stands for the residual terms growing slower than linearly in the norm of $\mathbf{x}$. In this case, the coefficients of B in the standard orthonormal bases of P and $P_\perp$ are

$$B = \begin{pmatrix} Z+X & -Y \\ -Y & Z-X \end{pmatrix}, \tag{17}$$

where (X,Y,Z) are the coordinates of the tiling in the 3D composition space given by the formulas in Eqs. 8b. Moreover, in this case

Table 1 Some special composition points

τ	N_t/N_s	Composition points	Example of phase
0	0	$\mathbf{S}_1, \mathbf{S}_2, \mathbf{S}_3$	pure phases of squares
$2\sqrt{3}-3 \simeq 0.464$	2	$\mathbf{\Sigma}_1$, $\mathbf{\Sigma}_2$, $\mathbf{\Sigma}_3$	Σ phase
$2\sqrt{3}-3 \simeq 0.464$	2	$\mathbf{H}_1$, $\mathbf{H}_2$, $\mathbf{H}_3$, $\mathbf{H'}_1$, $\mathbf{H'}_2$, $\mathbf{H'}_3$	H phase
$1/2 = 0.5$	$4/\sqrt{3}$	$\mathbf{O}$	maximally symmetric phases
$1/2 = 0.5$	$4/\sqrt{3}$	$\mathbf{A}_1$, $\mathbf{A}_2$, $\mathbf{A}_3$, $\mathbf{A'}_1$, $\mathbf{A'}_2$, $\mathbf{A'}_3$	aperiodic striped phases
1	∞	$\mathbf{T}_{13}, \mathbf{T}_{24}$	pure phases of triangles

also holds the following identity:

$$\tau - \sigma = \det(B) = Z^2 - X^2 - Y^2. \tag{18}$$

A detailed proof of this proposition is given in †ESI file part B. It is instructive to compare the situation of a general globally uniform tiling with that of the pure phases. As follows from (16), the lifted version of a globally uniform tiling follows asymptotically the direction of a 2D-plane $P_B \in P \oplus P_\perp$ with the hyperslope given by the matrix B. However, except of the case of the pure phases, the lifted tiling forms a corrugated surface, as the lifted vertices are not located in the same 2D-plane. In practice, for a globally uniform tiling, the relation between its composition and the hyperslope (eq. 17) can be written in an equivalent form as an average over the different types of tiles as follows (eq. 19) by using the hyperslopes of the pure phases (see Table 2) :

$$B = \sigma_1 B^{S1} + \sigma_2 B^{S2} + \sigma_3 B^{S3} + \tau_{13} B^{T13} + \tau_{24} B^{T24}. \tag{19}$$

Since all matrices B^Φ are symmetric, the matrix B is symmetric. Moreover, its coefficients are related to the (X,Y,Z) coordinates in a simple way.

The lifting construction also allows for a simple demonstration of the Nienhuis relation stated in section 2.2. We previously assumed this relation following the literature.[24] The presence of quadratic terms in the surface area of tiles comes from the expression of the determinant of the matrix B (Eq. 18) and Eq. 11 is obtained directly. The Nienhuis relation (Eq. 6) follows immediately from the latter along with the barycentric relations in Eqs (8b).

Historically, square-triangle tilings were introduced as models for quasicrystals with 12-fold symmetry. In this context, the point **O** at the center composition space with $X = Y = Z = 0$ has a special significance and corresponds to the maximally symmetric phases as developed in Section 5.4. Since any deviation of the hyperslope from zero breaks the average 12-fold symmetry, by a mechanical analogy the matrix B is commonly called the "global phason strain", the term coined by C. Henley in[21,30]. Here we consider all possible compositions, and do not restrict ourselves to the vicinity of the center of the composition space.

5 Some special phases

Here we focus on some special phases of interest for soft matter systems. Their location in the 3D composition space is given in Table 1. Note that, apart from the trivial case of the five "pure phases" previously discussed, in general, a given point in the 3D composition space corresponds to an infinite number of possible phases. In this section, we will start by the simplest case of the periodic Archimedean phases (section 5.1), that correspond to all the regular and semi-regular tilings made of squares and triangles, including the Σ phase (section 5.2). Then we will turn to the striped phases (section 5.3) which include both periodic phases (like the Archimedean H phase) and 1D quasi-crystalline phases. Last but not least, the maximally symmetric phases located at the center of the 3D composition space are investigated (section 5.4).

Table 2 Hyperslopes B^Φ for the five "pure" phases (Eq. (13)

Pure phase Φ	B^Φ
$T13$	$\begin{pmatrix} 1 & 0 \\ 0 & 1 \end{pmatrix}$
$T24$	$\begin{pmatrix} -1 & 0 \\ 0 & -1 \end{pmatrix}$
$S1$	$\begin{pmatrix} 1 & 0 \\ 0 & -1 \end{pmatrix}$
$S2$	$\begin{pmatrix} -1/2 & -\sqrt{3}/2 \\ -\sqrt{3}/2 & 1/2 \end{pmatrix}$
$S3$	$\begin{pmatrix} -1/2 & \sqrt{3}/2 \\ \sqrt{3}/2 & 1/2 \end{pmatrix}$

5.1 Archimedean phases : pure phases, Σ and H phases

By definition, Archimedean tilings are periodic structures built from regular convex polygonal tiles that have only one kind of vertex. In total, there are eleven different Archimedean tilings of the plane. Three of them are the regular tilings made of only one type of tiles : triangle, square or hexagon. They include the already introduced "pure phases". The eight other Archimedean tilings are semi-regular tilings as they combine different types of regular tiles. Among them, only two combine square and triangle tiles and are usually named the 3^2434 and 3^34^2 tilings (Figure 8) in the literature, where the notation comes from the arrangement of the tiles around each vertex (see Figure 3). Here we will call them the Σ and H phases respectively, by analogy with the Frank and Kasper three dimensional structures known in metallic alloys and also encountered in soft matter systems.

The Σ and H phases are the simplest examples of periodic square-triangle phases with a number of triangles twice the number of squares in a unit cell. In the 3D composition space, they are located on the same constant τ-surface, with $\tau = 2\sqrt{3}-3 \simeq 0.464...$ (Table 1 and Figure 7) but at different composition points. In the H phase, all squares have the same orientation and are combined with triangles of the appropriate family. This phase is the simplest example of striped phases as discussed in section 5.3 later on and is made of a 1D periodic stack of alternate infinite stripes of squares and triangles. As the H phase may have six different in-plane orientations, it is encountered at six points ($\mathbf{H}_1$,

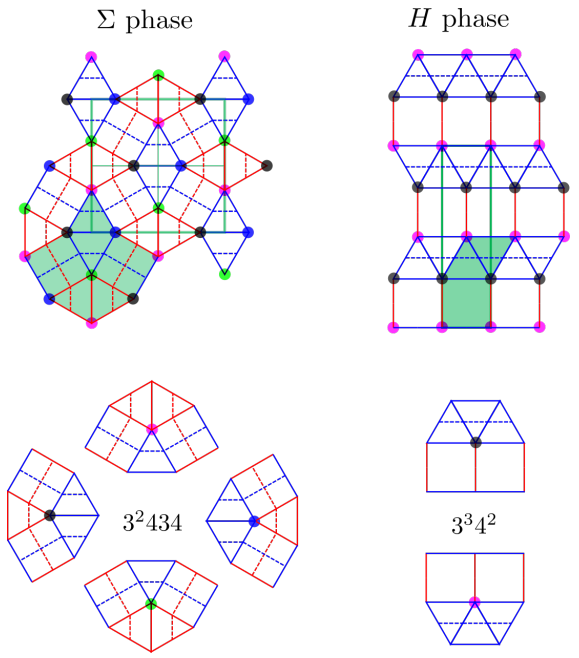

Fig. 8 The Σ phase and the H phase based on the two Archimedean tilings combining squares and triangles. The orientation of the tilings corresponds to the 3D composition points Σ_1 and $\mathbf{H}_1$. In green are shown elementary domains (two squares and four triangles for the Σ phase and one square plus two triangles for the H phase) from which the whole tiling can be built by successive translations. Conventional unit cells (square centered for the Σ phase and rectangle centered for the H phase) are depicted with green lines. Colors on vertices correspond to their different orientations which are shown at the bottom of the figure. Left : the four orientations (shown in black, blue, magenta and green) of the 3^2434 vertices. Right : the two orientations (shown in black and magenta) of the 3^34^2 vertices.

$\mathbf{H}_2$, $\mathbf{H}_3$, $\mathbf{H'}_1$, $\mathbf{H'}_2$, $\mathbf{H'}_3$) in the 3D composition space (see Table 1 and Figures 6 and 7). Assuming that in Figure 8 the squares are in the orientation S_1 and are combined with T_1 and T_3 triangles, the composition point is $\mathbf{H}_1$ with $X=\sigma_1=4-2\sqrt{3}$, $Y=0$ and $Z=\tau_{13}=2\sqrt{3}-3$.

The Σ phase is encountered at three different composition points ($\mathbf{\Sigma}_1$, $\mathbf{\Sigma}_2$, $\mathbf{\Sigma}_3$), corresponding to three possible in-plane orientations, deduced from each other by a rotation of $2\pi/3$ (Figures 6 and 7). In the Σ phase, the symmetry breaking in the tiles orientation affects only the square tiles, with only two orientations of squares present in the same amount. Composition point $\mathbf{\Sigma}_1$ (see Figure 6) is located in the OXY plane along the OX axis at $X=\sqrt{3}-2\simeq-0.268$, at the intersection with the surface of equation $\sigma_1=0$. Its composition is $\tau_{12}=\tau_{34}=(2\sqrt{3}-3)/2\simeq0.23205$, $\sigma_2=\sigma_3=1/(2+\sqrt{3})\simeq0.26795$ and $\sigma_1=0$. In the next section, we investigate more deeply the geometrical feature of the Σ phase.

5.2 Σ phase

As expected for an Archimedean tiling, the arrangement of tiles around each vertex of the Σ phase is fixed. All vertices are 3^2434 vertices (Figure 3) with four possible in-plane orientations pictured with four different colors (blue, black, green and magenta) in figures 8, 9 and 10. Each set of vertices having the same color forms a regular square lattice so the whole tiling can be decomposed in four identical subsets of vertices translated from each other. It is interesting to examine the lifted version of the Σ phase. The whole derivation is given in †ESI file part C.1. As a result, the decomposition into four regular square lattices is kept in the lifted version in 4D space. Indeed, the lifted 4D vertices are located in four 2D-planes parallel to each other, each 2D-plane containing the vertices with the same orientation (same color). These 2D-planes share the same hyperslope B^{Σ} (composition point $\mathbf{\Sigma}_1$ with $X=\sqrt{3}-2, Y=0, Z=0$, see Eq. 17):

$$B^{\Sigma}=\begin{pmatrix}-(2-\sqrt{3}) & 0\\ 0 & 2-\sqrt{3}\end{pmatrix} \tag{20}$$

In Figure 9, the two projections of the lifted Σ phase in the P and $P_\perp$ planes are shown. These two projections are complementary views of the 4D-vertices of the lifted Σ phase. Both exhibit the same periodic infinite tiling of the Σ phase but with a size ratio of $(2-\sqrt{3})$ between the projections from P to $P_\perp$, a ratio related to the non-zero coefficient in the matrix B^{Σ} (see Eq. 20).

Another useful way to characterise the Σ phase is to derive its 2D structure factor (see Figure 10 and †ESI file part C.1). The Bragg diffraction peaks are located on a periodic square lattice and exhibit strong modulations in their relative intensities. Moreover, some sets of Bragg peaks show an approximate 12-fold symmetry. This illustrates the fact that the Σ phase is an "approximant" phase of a dodecagonal quasicrystal, following the usual terminology of quasicrystals. Other approximant phases with larger unit cells[31] can be built and the symmetry of their structure factor gets even closer to a perfect 12-fold symmetry (ESI file E.2).

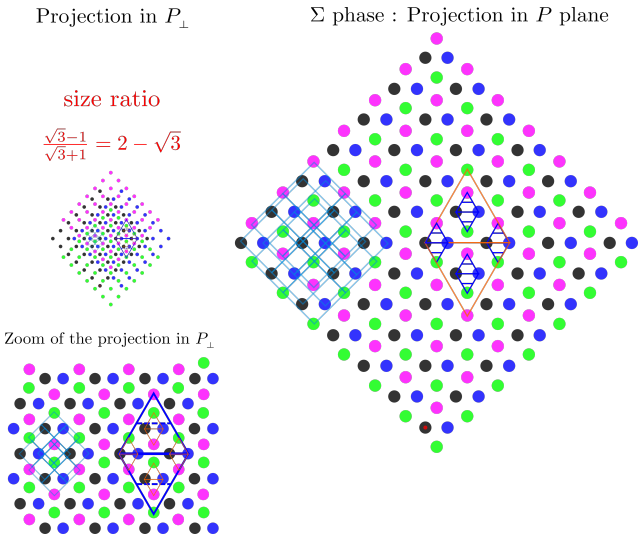

Fig. 9 Projections in the planes P (right hand side) and $P_\perp$ (left hand side) of the 4D lifted Σ phase. Both projections give the same periodic pattern but with a size ratio of $2-\sqrt{3}$ from P to $P_\perp$. A zoom view of the projection in $P_\perp$ is shown at the bottom left of the Figure. The four square lattices formed by each type of vertex orientation (blue, magenta black and green disks) are indicated in light blue lines. Triangles in blue and orange colors illustrate how the two projections of a given 4D vertex in P and $P_\perp$ are related. Globally, the green and magenta vertices exchange their positions along the vertical direction (see Figure 23 in †ESI file).

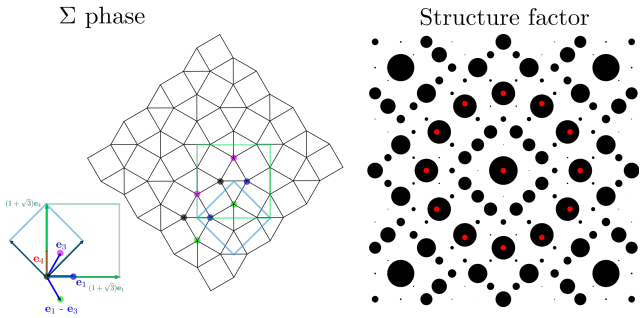

Fig. 10 (left) Σ phase with a square primitive unit cell outlined in blue (4 vertices) and a square centered unit cell in green (8 vertices). The edge's size of the centered square unit cell is $a_\Sigma = a(1+\sqrt{3})$ where a is the edge's size of the tiles. (right) Structure factor of the Σ phase. Spots are located on a square lattice and their radii are proportional to the diffraction peak intensities. For one of such set, an approximate 12-fold symmetry is observed. Red points with a strict 12-fold symmetry are added to help visualising the tiny difference in the peak positions. Differences in the intensity values between these 12 peaks are much too small (less than 1 percent) to be easily detected (see †ESI file part C.1).

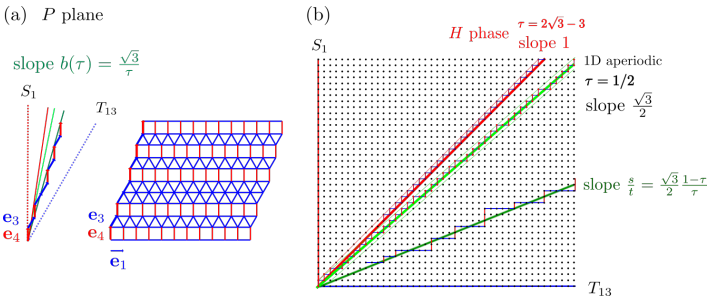

Fig. 11 Striped phases. (a) In the plane P, one vector ($\mathbf{e}_1$) corresponds to the periodicity along the stripes when the two other ones ($\mathbf{e}_3$, $\mathbf{e}_4$) define the stacking sequence. The average slope $b(\tau) = \frac{\sqrt{3}}{\tau}$ is directly linked to the composition via the parameter τ. (b) Different stacking sequences shown in a square lattice. The average slope is the stripe's ratio s/t. For the H phase, the average slope is equal to one. For $\tau = 1/2$, the sequence is aperiodic and is obtained via an inflation procedure (see Figure 12). In a random sequence (bottom right), the probability p of triangular stripes is fixed by the composition with $(1-p)/p = s/t$.

Lastly, let's us underline that, contrary to pure phases, the Σ phase is not the only possible phase at its composition point. By applying a simple transformation to the tiles (see †ESI file part C.1), it is possible to generate an infinite sequence of phases sharing the same composition. Note that all these periodic phases are globally uniform and cannot be generated by a cut-and-project method. Interestingly, the infinite limit of this transformation corresponds to the coexistence of four domains of pure phases (see section 6.2) around a junction point.

5.3 Striped phases

Striped phases are found all along the red lines which lie on the edges of the allowed region $\mathscr{V}$ (Fig. 6). They consist of squares and triangles of only one orientation, like the S1 tiles combined with the T1/T3 tiles (red line joining points $\mathbf{S}_1$ and $\mathbf{T}_{13}$). Stacks of infinite stripes of squares or triangles is the only way to assemble such tiles. Consequently, striped phases are periodic in the direction parallel to the strips; however, in the perpendicular direction, there are no restrictions on the stacking sequence, which can be periodic, aperiodic or disordered. The simplest example of a periodic striped phase is the alternation of one stripe of squares and one stripe of triangles and it corresponds to the Archimedean H phase (section 5.1 and Fig. 8).

In terms of composition, in contrast with the general case where three parameters (X,Y,Z) are needed, the composition of a striped phase is fixed by only one parameter, e.g. τ, the area fraction occupied by the triangular tiles introduced in section 2.2. Indeed, along the red line joining $\mathbf{S}_1$ and $\mathbf{T}_{13}$, the composition is given by $\tau = \tau_{13}$, with $\sigma = \sigma_1 = 1-\tau_{13}$ or $X = 1-\tau$, $Y = 0$, $Z = \tau$. The expression of the hyperslope B (Eq. 19) is a combination of the two pure phases B^{T13} and B^{S1}:

$$B = \begin{pmatrix} 1 & 0 \\ 0 & 2\tau-1 \end{pmatrix} = \sigma B^{S1} + \tau B^{T13} = (1-\tau)B^{S1} + \tau B^{T13} \quad (21)$$

The matrix is diagonal and the hyperslope depends only on a single parameter τ. With only one parameter to fix the composition, the lift construction is much more simple. When lifted in the 4D space, a striped phase looks like a "staircase' or a corrugated sheet (†ESI file part C.3). To fully characterise a striped phase, only its stacking sequence is needed.

The most direct way to visualise the stacking sequence is inside the plane P (Fig. 11a). One vector corresponds to the periodicity along the stripes when the two other ones define the stacking sequence. The stack of the stripes is given by a sequence of vectors $\mathbf{e}_3$ (stripe of triangular tiles) and $\mathbf{e}_4$ (stripe of square tiles) that follows a straight line of slope $b(\tau) = \sqrt{3}/\tau$ (ESI file C.3.1). It is noteworthy that the slope fixes the overall composition but not the stacking sequence. Indeed, at any composition point (fixed τ value), an infinite number of stacking sequences is possible (except for the two pure phases for $\tau = 0$ and $\tau = 1$). To satisfy the global uniformity condition, some lattice points in a stack sequence may be located far away of the straight line, but in such a way that the average slope is followed at a global scale.

A convenient way to visualise any of these stacking sequences is by encoding the successive stripes to form a broken line on a square lattice (Fig. 11b). The average slope of the line is s/t for a finite sequence of s stripes of S1 squares and t stripes of T1-T3 triangles. The relationship between s/t and τ is given by:

$$\frac{s}{t} = \frac{2N_s}{N_t} = \frac{\sqrt{3}}{2}\frac{1-\tau}{\tau} \quad (22)$$

An advantage of this representation is that the pure phases (all triangles or all squares) lie along the horizontal and vertical axes and the H phase corresponds to a slope equal to 1 (see †ESI file part C.3). This representation using a square lattice is commonly used for 1D aperiodic order.[26] A straight line of rational slope contains a periodic set of lattice points and describes in particular periodic phases. In contrast, aperiodic phases are encountered when the slope is irrational and no lattice points other than the origin are located on the straight line.

The slope equal to $\frac{\sqrt{3}}{2}$ in Figure 11b is of particular interest as it corresponds to the composition point $\mathbf{A}_1$ located on the conical

τ-surface for $\tau = 1/2$ (Figs 6 and 12). An explicit way to construct a 1D aperiodic phase for this composition is to use an inflation procedure based on a substitution rule.[32] As illustrated in Figure 12, by repeating the substitution rule (given in †ESI file part D.1), the irrational slope is approximated step by step by a sequence of rational numbers getting closer and closer to the non-periodic limit case. Each step in the inflation procedure corresponds to a periodic stack, with τ getting closer and closer to $1/2$ and s/t closer and closer to $\sqrt{3}/2$. Thus, in the limit of an infinite number of iterations, a 1D aperiodic sequence with $\tau = 1/2$ is obtained. The first three iteration steps of the inflation are shown in Fig. 12b.

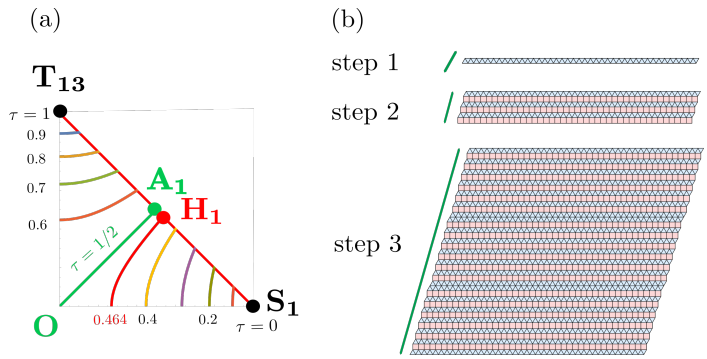

Fig. 12 Striped phases. (a) In the Oxz plane of the 3D space, they are located all along the red line joining the point $\mathbf{S}_1$ and $\mathbf{T}_{13}$ (see Figure 6). Special composition points are shown along this line like point $\mathbf{H}_1$ corresponding to the H phase ($\tau = 0.464$, see Table 1) and point $\mathbf{A}_1$ corresponding to the intersection with the τ-surface for $\tau = 1/2$ (see Figure 7). (b) Construction by inflation of a 1D quasiperiodic striped phase of composition corresponding to point $\mathbf{A}_1$. The three first iteration steps are shown and the substitution rules for the two tiles are given in †ESI file part D.1). Each inflation step gives a stacking sequence which average slope (green line) gets closer and closer to the irrational value $\sqrt{3}/2$.

The above procedure produces aperiodic striped phases that are maximally uniform, for which the lifted tiling deviates the least from the average slope. The order of stripes in such phases is always given by a binary Sturmian sequence and is therefore unambiguously defined by the composition.[33] Alternatively to the inflation, Sturmian sequences can be produced by a cut-and-project scheme, a convenient approach to construct a maximally uniform striped phase of any composition. A well-known example of such constructions is the Fibonacci sequence (see †ESI file part E).

On the opposite side of the spectrum to the Sturmian sequences lie random striped phases. In these phases the sequence of stripes is given by a Bernoulli process, that is the type of each stripe is chosen at random with a fixed probability, depending of the average global composition. Note that in contrast to the 2D case discussed in the next section, the corresponding entropy is subextensive: it grows with the length L of the tiling along the aperiodic direction as $S \propto L$.

5.4 Maximally symmetric phases

The center of the composition space (point O) corresponds to 'maximally symmetric phases' where all allowed orientations for each type of tile (square or triangle) are equally frequent. This fixes the values of all the five area fractions (see Eq. 9) and the overall composition to $\tau = 1/2$. Because the ratio $N_t/N_s = 4/\sqrt{3}$ is irrational, maximally symmetric phases cannot be periodic, a very important property already encountered for the striped phases with $\tau = 1/2$ (section 5.3). The composition of a maximally symmetric phase is given by $X = Y = Z = 0$ and thus corresponds to zero hyperslope:

$$B^O = \begin{pmatrix} 0 & 0 \\ 0 & 0 \end{pmatrix} \tag{23}$$

Therefore, in the superspace, the lifted tiling remains globally close to the plane P which has the hyperslope B^O. As for any other composition point, there is an infinite number of different possible maximally symmetric phases. Moreover, the entropy density is maximal at this very composition.[17,22,23] In fact, in the literature, maximally symmetric phases often occur as solutions of random tiling models.[34,35]

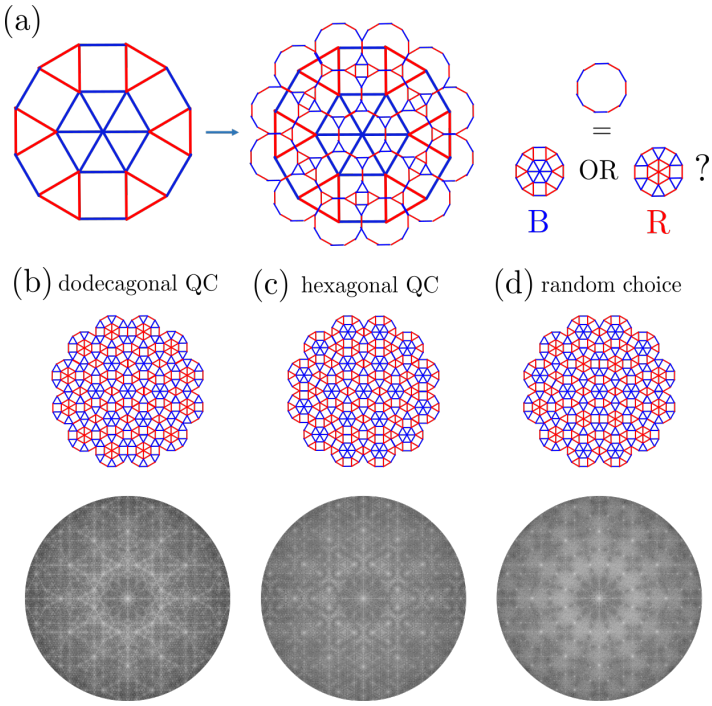

Fig. 13 Inflation method for maximally symmetric phases. (a) Initial seed is a dodecagonal wheel. At the first inflation step, 19 dodecagonal wheels are constructed on each vertices of the initial seed. Two different choices, B (blue) or R (red), are possible for the orientation of a wheel. Patches obtained after one inflation step are shown for (b) the dodecagonal QC phase (c) the hexagonal QC phase (d) a phase using a random choice between the B and R orientations. The Fourier transform of the patches obtained after two inflation steps is shown. For the two QC phases, either with 12-fold (b) or 6-fold symmetry (c), the pattern exhibits sharp diffraction peaks, whereas additional diffuse background in-between the peaks is present for the random choice (d).

The emblematic property of maximally symmetric phases is the dodecagonal symmetry. It should be emphasized that this prop-

erty holds only in the statistical sense, that is as a symmetry of *a class of globally uniform phases* corresponding to the composition point O, while none of the tilings is invariant itself with respect to the rotation of the plane by $\pi/6$. As a consequence, in maximally symmetric phases all six orientations for edges $(e_1, e_2, e_3, e_4, e_5, e_6)$ appear with equal frequency[36]. It is noteworthy that a small subset of maximally symmetric phases exhibit the dodecagonal symmetry in a stronger sense – that of the symmetry of the local isomorphism class[26], when the arbitrarily large regions of the tiling obtained by rotation can also be found in the original one. For instance, this is the case for the tilings corresponding to cut-and-project models with the acceptance windows having 12-fold symmetry (Figure 14 b, c).

In addition to rotational invariance, some quasicrystalline phases show self similarity: making a local transformation converts the tiling into an equivalent one with bigger tiles. It is thus possible to generate examples of maximally symmetric phases using inflation method, a method already introduced for the 1D striped quasiperiodic phases (see section 5.3). For 12-fold symmetry, different possible sets of seeds and substitution rules are available in the literature.[21,26,32,36–40] To illustrate this method, let's consider an initial seed in the form of a dodecagonal wheel as shown in Figure 13a. Note that the composition of this seed is maximally symmetric, with all area fractions in the adequate amount (see Eq. 9), but it cannot tile the plane without holes. At the first inflation step, dodecagonal wheels are placed on the 19 vertices of the seed. The gaps between them are filled in a unique way by triangles and squares and their orientations are maximally symmetric as well (see Figure 13a). All the tiles are then scaled up in length by a factor $2+\sqrt{3}$ to make them the same size as the original ones. The inflation rules are applied infinitely many times and patches of increasing sizes are generated at each step.

Each dodecagonal wheel can be placed with two possible orientations, labeled B (blue for the T1-T3 triangles) and R (red for the T2-T4 triangles). This freedom in the choice of orientation for each wheel (inside a patch and at each iteration step) allows to construct an infinite family of different maximally symmetric phases. To construct a perfect dodecagonal quasicristalline phase, a specific rule for the choice between B and R has to be applied at each inflation step which is given in the †ESI file part D.2).[32] This rule leads to the same dodecagonal QC as the so-called modified Schlottmann rules.[32,40] In Figure 13b, the patch obtained after one inflation step is shown. The Fourier transform for the patch after two iteration steps exhibits sharp diffraction peaks and 12-fold rotational symmetry, the signature of a perfect dodecagonal quasicrystalline order as explained at the end of this section.

Interestingly, if the inflation rule is defined by fixing the orientation of the wheels to be always the same, the resulting quasicrystalline phase (first discovered by Peter Stämpfli[37,40]) exhibits the hexagonal symmetry in the sense of the local isomorphism class[26]. This symmetry is evidenced by the Fourier transform (Fig. 13c). Lastly, flipping a coin to choose between the two orientations (B and R) for the dodecagonal wheels at *each site* gives rise to a disordered maximally symmetric phase (Fig. 13d). The diffraction pattern of this phase exhibits the 12-fold symmetry but with diffuse scattering present along with the Bragg peaks. Note that the entropy of this particular set of phases $S = \log(\Omega_N)$ grows linearly with the size of the system, since the number of B/R configurations of N dodecagons is given by $\Omega_N = 2^N$.

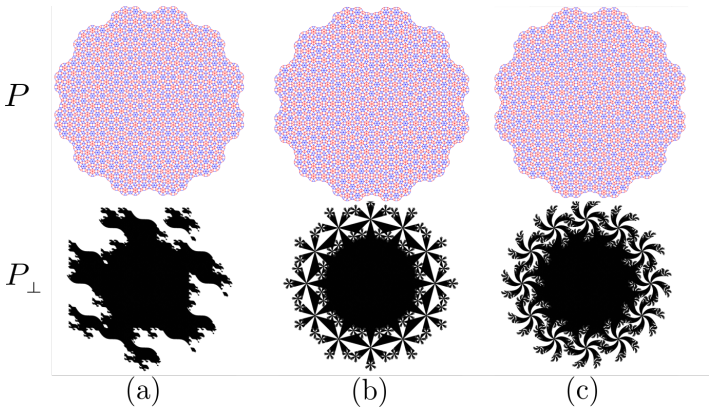

Fig. 14 Examples of perfect quasicrystalline phases among maximally symmetric phases. Patches in the plane P (after three inflation steps) are shown at the top and the corresponding acceptance windows (five inflation steps) in $P_\perp$ at the bottom. (a) Without rotationnal symmetry in the selection function (b) 12-fold symmetry for the Schlotmann QC dodecagonal tiling (also shown in Figure 13b (c) Another example with 12-fold symmetry with a different selection function.

In practice, when an experimental pattern is obtained, two analysis tools are helpful to assess the type of symmetry: the diffraction pattern and the plot of the vertices in the plane $P_\perp$ using the lift procedure. These two approaches are sensitive to the symmetry in different ways. The first approach originated in the physics of quasicrystals, where according to the common definition, a quasicrystal is characterised by its diffraction pattern, containing Bragg peaks indexed in a reciprocal space with a dimension greater than that of the structure[25]. In the present case, the Bragg peaks are indexed by four integers. A dodecagonal quasicrystal is then defined by the fact that its diffraction pattern contains Dirac-delta peaks and exhibits a perfect 12-fold symmetry, as illustrated by Figure 13b. It is worth mentioning here that the symmetry of the diffraction pattern may differ from that of the plane P_B, as illustrated by the hexagonal symmetry of Figure 13c. This can be understood from the example of tilings obtained as cut-and-project models (these phases correspond to the so-called perfect quasicrystals, characterized by pure point diffraction). For instance, the acceptance window of Figure 14a has no symmetry, and therefore the diffraction pattern of the corresponding tiling should not be symmetric either. This illustrates the fact that the symmetry of the lifting construction in general does not reflect the symmetry (or even the nature) of the diffraction pattern, although it is conjectured that the maximally symmetric phases originated as random tilings exhibit symmetric diffraction patterns with Bragg peaks along with some additional diffuse scattering, as illustrated in Figure 13d[34].

The plot of the vertices in the plane $P_\perp$ also gives helpful information about the symmetry of an experimental pattern.[19,27] To illustrate this point, several examples of quasiperiodic phases are shown in Figure 14. As these examples are constructed by inflation, the projection of the 4D vertices in the $P_\perp$ is of finite

width around the origin and it is usually called the acceptance window in the literature. A remarkable property is that these acceptance windows have a fractal border (see Figure 14) [32,36,41]. For a more disordered maximally symmetric phase (not obtained by inflation) the projection in $P_\perp$ may be not bounded. This is related to the fact that, if one considers finite clusters of larger and larger size R, the number of cluster-types grows with R following a power-law for a perfectly quasiperiodic phase when it grows exponentially with R for more disordered phases.

In conclusion, it is still an open challenge to establish whether the dodecagonal phases encountered in soft matter systems correspond to maximally symmetric phases rather than long-range quasicrystalline order evidenced by pure point diffraction.

6 Grain boundaries: When global uniformity is absent

The global uniformity condition (see section 4.2) may be too restrictive for real experimental systems which may contain domains of different compositions. In this section, we shall see how the "irrotational property" (Eq. 15) leads to constraints on the coexistence of locally uniform domains. we derive precise rules for the coexistence of such domains and are able to make some predictions on their phase behavior. It should be emphasized that near the domain boundaries a tiling considered in this section still consists of squares and triangles only and is in this aspect *defect-free*. In the conclusion (section 7) we shall discuss the role of defects in real systems.

6.1 Coexistence of domains with different compositions

Let us start by relaxing the global uniformity condition introduced in section 2.2 (see Figure 4). Namely, let us consider a possible not-globally uniform tiling containing two locally uniform domains. More specifically, we shall assume that any sequence of growing patches $\mathscr{P}_i$ satisfying the condition (Eq. 2) is a disjoint union of two sub-patches

$$\mathscr{P}_i = \mathscr{P}'_i \sqcup \mathscr{P}''_i$$

also satisfying the condition (Eq. 2) and having a well-defined limit of the area fractions (Eq. (3)). Let us denote the coordinates of the corresponding points in the composition space by (X',Y',Z') and (X'',Y'',Z'') respectively. Inside each domain the formula (16) still holds, for the matrix B taking the respective values B' and B''. The continuity of the lifting map then yields the following condition on the boundary between the sub-patches

$$B'' \cdot \mathbf{x} - B' \cdot \mathbf{x} = o(|\mathbf{x}|) \tag{24}$$

where $\mathbf{x}$ is a point at the boundary.

Since the boundary between the domains is unbounded, the condition (24) means that

$$\det(\delta B) = 0, \tag{25}$$

where $\delta B = B'' - B'$. Let $(\delta X, \delta Y, \delta Z)$ stand for the difference of the barycentric coordinates of two domains:

$$\begin{pmatrix} \delta X \\ \delta Y \\ \delta Z \end{pmatrix} = \begin{pmatrix} X'' \\ Y'' \\ Z'' \end{pmatrix} - \begin{pmatrix} X' \\ Y' \\ Z' \end{pmatrix} \tag{26}$$

Then

$$\delta B = \begin{pmatrix} (\delta Z + \delta X) & -\delta Y \\ -\delta Y & (\delta Z - \delta X) \end{pmatrix} \tag{27}$$

and the condition (25) reads as

$$(\delta Z)^2 = (\delta X)^2 + (\delta Y)^2 \tag{28}$$

Therefore, two domains of different composition may be in contact along an infinite frontier only if the difference of the corresponding barycentric coordinates satisfies the condition (28). In the 3D composition space, this condition can be visualized by a conical surface like the τ-surface for $\tau = 1/2$ but centered on the point (X',Y',Z') instead of the origin (see Figures 7 and 16a). Any composition point (X'',Y'',Z'') located on this conical surface may be in coexistence with the composition (X',Y',Z').

A remarkable consequence of the constraint (28) is that a locally uniform domain with $\tau > 1/2$ may not be in contact with a domain with different barycentric coordinates but having the same value of τ. Indeed, as follows from (11), equation (28) has no solution with two different points (X',Y',Z') and (X'',Y'',Z'') belonging to the same τ-surface if $\tau > 1/2$ (Figure 16a). Therefore a square-triangle tiling having a well-defined area fraction of triangles larger than $1/2$ *must be globally uniform*. On the other hand, phases with the same value of $\tau \leq 1/2$ may coexist, as illustrated by Figure 15. This case includes in particular the coexistence of two domains of aperiodic phases ($\tau = 1/2$) with a different symmetry, as for instance a maximally symmetric phase and a striped phase (Figure 15b). Of course, many other situations of coexistence may be encountered.

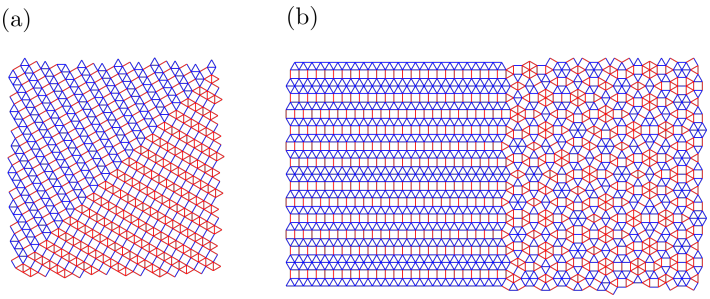

Fig. 15 Coexistence of two domains for (a) the H phase ($\tau = 2\sqrt{3}-3 = 0.464...$) and (b) aperiodic phases ($\tau = 1/2$) with a striped phase and a maximally symmetric phase.

6.2 Constraints on the domain boundaries

As follows from Eq. 24, the boundary between two infinite locally uniform domains is asymptotically close to the straight line defined by the following equation on $\mathbf{x} \in P$:

$$\delta B \cdot \mathbf{x} = 0, \tag{29}$$

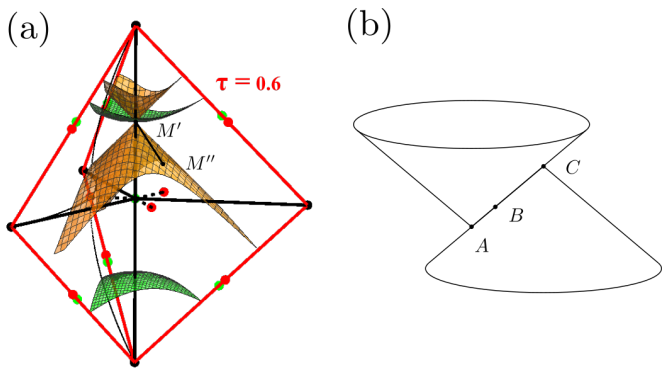

Fig. 16 Coexistence of domains in the 3D parameter space. (a) The point M' is on the τ-surface in green with $\tau > 1/2$ (similar representation as in Figure 7). The conical surface in orange corresponds to the coexistence condition of Eq. 28. Any composition point M'' located on it may give a domain in coexistence with composition M'. Because the intersection between the two surfaces in green and orange is reduced to point M', any square-triangle phase with $\tau > 1/2$ is globally uniform. (b) Three points A, B and C in the 3D composition space which may form pair-wise domain boundaries. The two conical surfaces represent the coexistence condition applied to the vectors $B-A$ and $B-C$ respectively. The points A, B and C must be colinear.

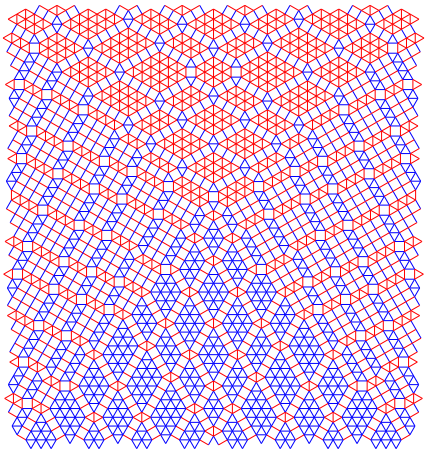

Fig. 17 Junction point between locally uniform domains : four is the minimum number of domains as illustrated here.

where δB is given by Eq. 27. Let α stand for the angle between the unit vector $\mathbf{n}$ normal to this line and the direction of the vector $\mathbf{e}_1$:

$$\mathbf{n} = \begin{pmatrix} \cos\alpha \\ \sin\alpha \end{pmatrix}$$

For a fixed $\mathbf{n}$, we can consider (29) as an equation on δB. With the parametrization (27), this equation admits solutions of the form

$$\begin{pmatrix} \delta X \\ \delta Y \\ \delta Z \end{pmatrix} = c \begin{pmatrix} \cos(-2\alpha) \\ \sin(-2\alpha) \\ 1 \end{pmatrix}, \qquad (30)$$

where c is a real parameter. Equation (30) thus establishes the one-to-one correspondence between the vector $(\delta X, \delta Y, \delta Z)$ (Eq. 26) in the concentration space and the direction of the corresponding domain boundary.

Let us now consider the situation of pairwise coexistence of several locally uniform domains. Let us start with the case of three domains, corresponding to the points A, B and C in the concentration space. Without loss of generality, we can assume that following order of Z coordinates of the three phases:

$$Z_A \leq Z_B \leq Z_C.$$

Then, the condition (28) applied to the phases A and B constrains the point B to an upward-directed cone with the apex A (see Figure 16b). The point C must also belong to the same cone. In the same time, the point B is also constrained to a downward-directed cone with the apex C. This is only possible if all three points are colinear. By virtue of equation (30), this leads to the remarkable result that all three domain boundaries must be parallel, which precludes the existence of triple points of contact between locally uniform domains. Thus, *the simplest case of several domain boundaries joining together corresponds a quadruple junction* as illustrated in Figure 17.

7 Summary and perspectives

The huge diversity of square-triangle phases may be surprising at first sight considering the simplicity of the two tiles. This work explains how this very rich phase behavior derives from geometrical rules. Among them, the inherent incommensurability of the areas of the two tiles is essential. Combined with the fact that four different types of vertices (see Fig. 3b) provide plenty of possible ways to assemble the tiles and one can understand better the rich phase behavior for binary mixtures of squares and triangles. In this paper we propose a classification of these phases by means of a three-dimensional "composition space". The key ingredient in our approach is the notion of global uniformity, or the well-definedness of the seven area fractions occupied by tiles of different shapes and orientation. Fortunately, these quantities are linked by several constraints, leaving us only with three free parameters, which we use as the coordinates (X, Y, Z) in the 3D composition space. Fixing the global composition still leaves plenty of room for local rearrangements of tiles (except of the case of pure phases) and an infinite number of phases are sharing the same composition. All periodic phases are globally uniform as the composition can be defined in a unit cell, which has a finite extension. Moreover, global uniformity encompasses more disordered phases than the phases obtained by cut-and-project methods or inflation rules. For all cases, the three coordinates in the composition space suffice to characterize the global symmetry of a phase. The 3D composition space allows linking together all possible type of symmetries for square-triangle phases, in contrast to previous approaches focusing only on dodecagonal phases.

We introduce the term of maximally symmetric phases when the tiles are distributed in the most symmetrical way in terms of orientation. When maximizing the symmetry of the tiles orientation distribution, all the seven area fractions are fixed (see Eq. 9), corresponding to the center of the 3D composition space (point O). One of the most striking geometrical property of square-

triangle phases is that maximally symmetric phases can't be periodic but do offer aperiodic order instead. Maximally symmetric phases include dodecagonal quasicrystalline phases that can be generated by inflation methods, along with more disordered phases. Note that so far in soft matter systems, square-triangle phases are observed as finite patches of rather limited areas, making the distinction between a perfect quasicrystalline phase and a more disordered phase difficult to asses. Maximally symmetric phases also correspond to the maximum of the entropy density[22,23] and it is why it is often argued that they are entropically stabilised. This argument is correct, except that the overall composition of a binary mixture may be fixed at a value different from $\tau = 1/2$ and that the whole 3D-composition space needs to be considered, as discussed afterwards.

Moving apart from the center of the 3D composition space breaks the symmetry in the tiles orientation distribution. Our approach allows to identify all possible situations for such loss of symmetry, like a 3-fold symmetry along the OZ axis (Fig. 5b) or a 4-fold symmetry along the OX axis (Fig. 5c). The Σ phase is an important peculiar case for which the tiles orientation distribution is partially broken, with only one orientation missing for square tiles. Striped phases are a 1D limit case when the symmetry of the tiles orientation is entirely broken (as each tile has only one orientation) and only incommensurability matters.

In practice, determining the overall composition of an experimental or a numerical square-triangle pattern in terms of the (X, Y, Z) coordinates is straightforward and may be performed by direct image analysis. Providing that all edges in a pattern are oriented along the $\mathbf{e_i}$ directions, the tiles orientation distribution may be calculated for any finite area, providing the values of X, Y, Z and τ, allowing to locate the phase in the 3D-composition space. Global uniformity can be tested doing image analysis at different length scales, revealing at the same time possible coexistence of phases, grain boundaries or composition gradients.

Lifting an observed pattern in the 4D superspace and plotting its vertices both in the observation plane P and in $P_\perp$ is a powerful analysis tool as well. The lift construction is essential if one wishes to understand more deeply why the composition space has only three dimensions. Indeed, the central notion in the lifting scheme is the link between the average composition (X, Y, Z) and the hyperslope of a 2D-plane (symmetric 2x2 matrix B with three independent coefficients, see Eq. 17). This fact was introduced in the first place by C. Henley and coworkers[21,30] with the matrix B under the denomination of global phason strain, a term which is still largely used in the literature. In this work, we underline that this geometrical interpretation of the average composition by an hyperslope is valid in all the 3D composition space and not only close to its center. Moreover, we use it to derive a demonstration of the Nienhuis relation (Eq. 6), another way to introduce the fact that only three parameters are needed.

Let's discuss now some possible perspectives of this work that could be addressed in the near future for soft matter systems:

- The localisation of the Archimedean periodic Σ phase inside the 3D composition phase gives clues to understand its stability. There are many experimental observations of the Σ phase and it is generally a good sign that a dodecagonal phase could be stabilised as well in a given experimental system.[42] Our geometrical approach allows to clarify the relationship between the Σ phase with respect to maximally symmetric phases. Indeed, the Σ phase occurs at a precise composition $\tau = 2\sqrt{3} - 3 = 0.464$, which is slightly different but quite close to $\tau = 1/2 = 0.5$. Stability of the Σ phase may be attributed to the maximisation of the tiles orientation distribution at a fixed value of $\tau = 0.464$ as shown by the positions of the three composition points ($\mathbf{\Sigma}_1$,$\mathbf{\Sigma}_2$, $\mathbf{\Sigma}_3$) on the τ-surface with $\tau = cste = 0.464$. A fine tuning of the overall composition of a binary system may stabilise the Σ phase instead of a maximally symmetric phase.

- When τ is different from $1/2$, an open question is to determine if a phase separation between a maximally symmetric phase and pure phases (made of the excess of triangles or squares) is favoured or if symmetry breaking takes place instead. Solving this question would be a good test of the entropic stabilisation argument for dodecagonal phases. This question could be addressed by varying the value of τ experimentally in binary mixtures such as mixtures of spherical particles with two sizes[18] or mixtures of square and triangular nanoplatelets[43]. A delicate point would be to make sure that equilibrium states are reached to avoid such systems to be trapped in out-of-equilibrium states. More generally, the intuitive rule that equilibrium states correspond to phases with a maximal symmetry at a given τ value needs to be tested. Possible strategies could consist in promoting symmetry breaking experimentally. This could be done in many ways for soft matter systems : confinement or border effects, anisotropy via surface treatment or application of external fields. Following the nucleation/growth of square/triangle phases could also involve symmetry breaking effects.

- So far we consider only phases without defects, but defects are present and play an important role on the physical properties of real experimental systems. A first class of defects are grain boundaries. In this work, we give predictions about the coexistence of domains that may be confronted to future experimental observations. The coexistence of two domains obeys different rules for $\tau > 1/2$ (globally uniform phase only) and $\tau \leq 1/2$ (coexistence of domains with the same τ value). Geometrical rules for the junction of domain boundaries are predicted, with at least four domains around a junction point. As a perspective of this work, incorporating topological defects based on thin rhombus tiles (or shield tiles) would be a challenging extension of our approach.[29] These defects are typical to square-triangle tilings and their dynamic is related to the so-called "zipper" lines.[21] A few examples of quasiperiodic tilings made of square-triangle-rhombus tiles are known like the Niizeki–Gähler tiling[44,45] or the recent Schaad-Stampfli tiling[46]. Thin rhombus tiles are built using two successive edges directions like ($\mathbf{e_1}$, $\mathbf{e_2}$). Taking them into account would add six extra tiles, including orientation. These tiles are intimately related to square-triangle tilings because they are already included in the 4D

lattice. The restriction on the symmetry of the B matrix is vanishing when thin rhombus tiles are included, leading to the possibility to have any 2x2 matrix with four different coefficients for the hyperslope. In other words, the irrotationnal property is lost. Of course, three dimensions for the composition space wouldn't be appropriate but the selection rules in the 4D space may be simplified as any hyperslope could be accessible. Approaches to incorporate such topological defects are also stimulated by the recent discovery of 2D inorganic dodecagonal materials.[45]

In this work we have introduced a number of methods used in condensed matter physics to describe quasicrystals, but not yet popular in other fields such as soft matter or material chemistry. They should help addressing further challenges such as understanding the growth process of dodecagonal metamaterials[14] or the 2D self-assembly of binary mixtures of square and triangular nanoplatelets[43]. More experimental and numerical simulation results are now needed to explore the infinitely rich phase behavior of square-triangle phases.

Author Contributions

All authors have contributed to write and revise the manuscript.

Conflicts of interest

There are no conflicts of interest to declare.

Acknowledgements

We are grateful for many scientific discussions to Etienne Fayen, Giuseppe Foffi, Frank Smallenburg (LPS, Laboratoire de Physique des Solides, CNRS, Unversité Paris-Saclay, Orsay, France) and to Thomas Fernique (LIPN, CNRS, Université Paris-13, Villetaneuse, France). This work is funded by the French National Research Agency in the framework of the SoftQC project (ANR grant ANR-18-CE09-0025 at https://softqc.wordpress.com).

Notes and references

1 X. Zeng, G. Ungar, Y. Liu, V. Percec, A. E. Dulcey and J. K. Hobbs, *Nature*, 2004, **428**, 157–160.
2 G. Ungar and X. Zeng, *Soft Matter*, 2005, **1**, 95.
3 R. Zhang, X. Zeng and G. Ungar, *Journal of Physics: Condensed Matter*, 2017, **29**, 414001.
4 A. J. Mueller, A. P. Lindsay, A. Jayaraman, T. P. Lodge, M. K. Mahanthappa and F. S. Bates, *Macromolecules*, 2021, **54**, 2647–2660.
5 C. Xiao, N. Fujita, K. Miyasaka, Y. Sakamoto and O. Terasaki, *Nature*, 2012, **487**, 349–353.
6 Y. Sun, K. Ma, T. Kao, K. A. Spoth, H. Sai, D. Zhang, L. F. Kourkoutis, V. Elser and U. Wiesner, *Nature Communications*, 2017, **8**, 252.
7 Y. Wang, Q. Deng, N. Fujita and L. Han, *Chemistry of Materials*, 2020, **32**, 5236–5245.
8 D. V. Talapin, E. V. Shevchenko, M. I. Bodnarchuk, X. Ye, J. Chen and C. B. Murray, *Nature*, 2009, **461**, 964.
9 H. Zhao, R. P. Zaccaria, J.-f. Song, S. Kawata and H.-b. Sun, *Physical Review B*, 2009, **79**, 115118.
10 J.-W. Dong, K. H. Fung, C. T. Chan and H.-Z. Wang, *Physical Review B*, 2009, **80**, 155118.
11 S.-C. Cheng, X. Zhu and S. Yang, *Optics Express*, 2009, **17**, 16710.
12 M. N. van der Linden, J. P. K. Doye and A. A. Louis, *The Journal of Chemical Physics*, 2012, **136**, 054904.
13 X. Ye, J. Chen, M. E. Irrgang, M. Engel, A. Dong, S. C. Glotzer and C. B. Murray, *Nature Materials*, 2017, **16**, 214–219.
14 M. Zu, P. Tan and N. Xu, *Nature Communications*, 2017, **8**, 2089.
15 H. Pattabhiraman and M. Dijkstra, *Journal of Physics: Condensed Matter*, 2017, **29**, 094003.
16 C. N. Likos and C. L. Henley, *Philosophical Magazine B*, 1993, **68**, 85–113.
17 B. Nienhuis, *Physics Reports*, 1998, **301**, 271–292.
18 E. Fayen, A. Jagannathan, G. Foffi and F. Smallenburg, *The Journal of Chemical Physics*, 2020, **152**, 204901.
19 T. Ishimasa, S. Iwami, N. Sakaguchi, R. Oota and M. Mihalkovič, *Philosophical Magazine*, 2015, **95**, 3745–3767.
20 H. Kawamura, *Progress of Theoretical Physics*, 1983, **70**, 352–365.
21 M. Oxborrow and C. L. Henley, *Physical Review B*, 1993, **48**, 6966–6998.
22 M. Widom, *Physical Review Letters*, 1993, **70**, 2094–2097.
23 P. A. Kalugin, *Journal of Physics A: Mathematical and General*, 1994, **27**, 3599–3614.
24 J. de Gier and B. Nienhuis, *Physical Review E*, 1997, **55**, 3926–3933.
25 M. de Boissieu, *Acta Crystallographica. Section A, Foundations and Advances*, 2019, **75**, 273–280.
26 M. Baake and U. Grimm, *Aperiodic Order*, Cambridge University Press, 2013.
27 M. Baake, D. Ecija and U. Grimm, *Zeitschrift für Kristallographie - Crystalline Materials*, 2016, **231**, 507–515.
28 C. L. Henley, Proceedings of the Third International Conference on Quasicrystals, Vista Hermosa, Mexico, 1989, pp. 152–169.
29 M. Tsarenko, *PhD thesis*, University of Melbourne, Melbourne, 2013.
30 P. W. Leung, C. L. Henley and G. V. Chester, *Physical Review B*, 1989, **39**, 446–458.
31 A. W. Huran, H.-C. Wang and M. A. L. Marques, *2D Materials*, 2021, **8**, 045002.
32 J.-F. Sadoc and R. Mosseri, *Structural Chemistry*, 2017, **28**, 63–73.
33 J. Berstel, *International Journal of Algebra and Computation*, 2002, **12**, 371–385.
34 C. L. Henley, *Quasicrystals*, WORLD SCIENTIFIC, 1991, vol. Volume 11, pp. 429–524.
35 C. Richard, M. Hoeffe, J. Hermisson and M. Baake, *Journal of Physics A: Mathematical and General*, 1998, **31**, 6385–6408.
36 D. Frettlöh, *Symmetry: Culture and Science*, 2011, **22**, 237–246.
37 P. Stämpfli, *Helvetica Physica Acta*, 1986, **59**, 1260–1263.

38 J. Hermisson, C. Richard and M. Baake, *Journal de Physique I*, 1997, **7**, 1003–1018.

39 X. Zeng and G. Ungar, *Philosophical Magazine*, 2006, **86**, 1093–1103.

40 D. Frettlöh, E. Harriss and F. Gähler, *Tilings Encyclopedia*, 2020, `http://tilings.math.uni-bielefeld.de`.

41 M. Baake, R. Klitzing and M. Schlottmann, *Physica A: Statistical Mechanics and its Applications*, 1992, **191**, 554–558.

42 T. M. Gillard, S. Lee and F. S. Bates, *Proceedings of the National Academy of Sciences*, 2016, **113**, 5167–5172.

43 K. C. Elbert, W. Zygmunt, T. Vo, C. M. Vara, D. J. Rosen, N. M. Krook, S. C. Glotzer and C. B. Murray, *Science Advances*, 2021, **7**, eabf9402.

44 N. Niizeki and H. Mitani, *Journal of Physics A: Mathematical and General*, 1987, **20**, L405–L410.

45 S. Schenk, E. M. Zollner, O. Krahn, B. Schreck, R. Hammer, S. Förster and W. Widdra, *Acta Crystallographica Section A: Foundations and Advances*, 2019, **75**, 307–313.

46 T. P. Schaad and P. Stampfli, *arXiv:2102.06046 [math]*, 2021.

Table of contents : Here we present a way to describe all possible globally uniform square-triangle phases using a three dimensional composition space.

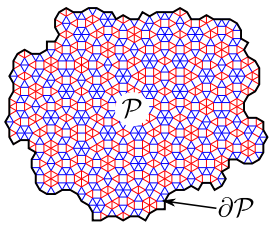

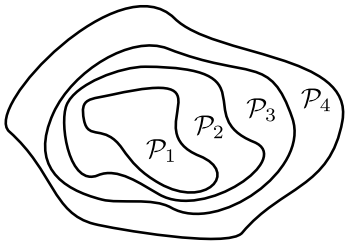

Electronic Supplementary Information file

Square-triangle tilings : An infinite playground for soft matter

Marianne Impéror-Clerc,*[a] Anuradha Jagannathan,[a] Pavel Kalugin,[a] and Jean-François Sadoc[a]

A Lift in 4D

A.1 Geometry in 4D

Here are introduced a few useful geometrical features of the Euclidean space in four dimensions. In a 4D orthonormal basis of four unit vectors, labelled $(\mathbf{I},\mathbf{J},\mathbf{K},\mathbf{L})$, any 4D-vector $\mathbf{X}$ has four coordinates:

$$\mathbf{X} = x\mathbf{I} + y\mathbf{J} + x_\perp\mathbf{K} + y_\perp\mathbf{L} \tag{31}$$

A 2D-plane of the 4D space is defined by two non-colinear 4D-vectors through the origin. To the orthonormal basis, a set of six 2D-planes can be associated: $(\mathbf{I},\mathbf{J})$, $(\mathbf{I},\mathbf{K})$, $(\mathbf{I},\mathbf{L})$, $(\mathbf{J},\mathbf{K})$, $(\mathbf{J},\mathbf{L})$ and $(\mathbf{K},\mathbf{L})$. Among them, two orthogonal 2D-planes, $(\mathbf{I},\mathbf{J})$ and $(\mathbf{K},\mathbf{L})$ are selected to play a special role, as they are used to represent any 4D-vector $\mathbf{X}$ by its two projections onto them. It is this projection scheme that is used in the lift construction, keeping always the same two 2D-planes. The two sets of coordinates (x,y) and $(x_\perp,y_\perp)$ can be represented separately onto two Euclidean planes, labelled respectively P and $P_\perp$. The four-dimensional Euclidean space can be defined as the orthogonal direct sum $P\oplus P_\perp$ where the planes P and $P_\perp$ are two embedded 2D orthogonal subspaces. By extension, the 2D-plane in 4D containing the 4D-vectors of coordinates $(x,y,0,0)$ is also named P.

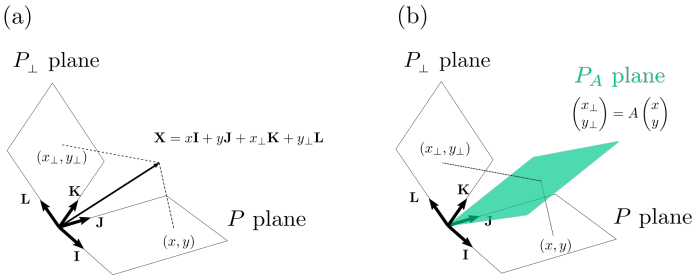

Fig. 18 Geometry in 4D: (a) 4D-vector (b) 2D-plane P_A and its hyperslope (given by a 2x2 matrix A) relative to the plane P.

In general, a 2D-plane P_A can be defined by the linear combination of two non-colinear 4D-vectors of coordinates (a,b,c,d) and (e,f,g,h) in the $(\mathbf{I},\mathbf{J},\mathbf{K},\mathbf{L})$ orthonormal basis. A 4D-vector is in the 2D-plane P_A if it is of the form:

$$\mathbf{X} = \begin{pmatrix} x \\ y \\ x_\perp \\ y_\perp \end{pmatrix} = \lambda \begin{pmatrix} a \\ b \\ c \\ d \end{pmatrix} + \mu \begin{pmatrix} e \\ f \\ g \\ h \end{pmatrix} \tag{32}$$

where λ and μ are two linear coefficients. This linear relation can be expressed equivalently as follows:

$$\begin{pmatrix} x_\perp \\ y_\perp \end{pmatrix} = A \begin{pmatrix} x \\ y \end{pmatrix} \tag{33}$$

where A is a (2x2) matrix:

$$A = \begin{pmatrix} A_{x_\perp x} & A_{x_\perp y} \\ A_{y_\perp x} & A_{y_\perp y} \end{pmatrix} = \begin{pmatrix} \frac{cf-bg}{af-be} & \frac{ag-ce}{af-be} \\ \frac{df-bh}{af-be} & \frac{ah-de}{af-be} \end{pmatrix} \tag{34}$$

The geometrical interpretation of the matrix A is the hyperslope of the 2D-plane P_A with respect to the plane P and it contains 4 coefficients in the general case. In a symmetric matrix, $A_{x_\perp y} = A_{y_\perp x}$ and only three independent coefficients are present. Such symmetric matrices are noted B in the main text.

Finally, we introduce a second orthonormal basis, $(\mathbf{I}',\mathbf{J}','\mathbf{K},\mathbf{L}')$, as it may simplify some relations :

$$\mathbf{I}' = \frac{\mathbf{I}+\mathbf{K}}{\sqrt{2}}, \mathbf{J}' = \frac{\mathbf{I}-\mathbf{K}}{\sqrt{2}}, \mathbf{K}' = \frac{\mathbf{J}+\mathbf{L}}{\sqrt{2}}, \mathbf{L}' = \frac{\mathbf{J}-\mathbf{L}}{\sqrt{2}} \tag{35}$$

A.2 4D lattice for the lift of square-triangle tilings

The standard construction of the lifting of a square-triangle tiling of the Euclidean plane P is detailed here following the literature.[21,27] Coming back to the six different orientations for edges (see Figure 2), one can observe that only four of six vectors $\mathbf{e}_1,\ldots,\mathbf{e}_6 \in P$ given by the formula (1) are linearly independent over $\mathbb{Z}$ (for instance, $\mathbf{e}_5 = \mathbf{e}_3 - \mathbf{e}_1$ and $\mathbf{e}_6 = \mathbf{e}_4 - \mathbf{e}_2$). Therefore, any vertex $\mathbf{v}$ of a square-triangle tiling is naturally indexed by 4 integers $n_1,\ldots,n_4$:

$$\mathbf{v} = \sum_{i=1}^{4} n_i \mathbf{e}_i. \tag{36}$$

as it belongs to the $\mathbb{Z}$-module of rang 4 spanned by the vectors $\mathbf{e}_1,\ldots,\mathbf{e}_4$. One can associate with the vertex $\mathbf{v}$ its counterpart $\mathbf{v}_\perp$ in another Euclidean plane $P_\perp$ (the so-called "inner" or "perpendicular" space) :

$$\mathbf{v}_\perp = \sum_{i=1}^{4} n_i \mathbf{e}_{i_\perp}, \tag{37}$$

where the vectors $\mathbf{e}_{i_\perp}$ have the following coordinates (in some fixed orthonormal basis of $P_\perp$):[21]

$$\mathbf{e}_{i_\perp} = a \begin{pmatrix} \cos\frac{7\pi(i-1)}{6} \\ \sin\frac{7\pi(i-1)}{6} \end{pmatrix} \tag{38}$$

The four-dimensional Euclidean space used for the lift construction is defined as the orthogonal direct sum $P\oplus P_\perp$. This space contains the planes P and $P_\perp$ as orthogonal two-dimensional subspaces. The "lifted" version of any vertex $\mathbf{v}$ is defined as the 4D-vertex $\mathbf{V} = (\mathbf{v},\mathbf{v}_\perp) \in P\oplus P_\perp$. Thus, the 4D vertices of the lifted tiling belong to a lattice spanned by four basis vectors $\boldsymbol{\varepsilon}_i = (\mathbf{e}_i,\mathbf{e}_{i_\perp})$ in $P\oplus P_\perp$:

$$\mathbf{V} = (\mathbf{v},\mathbf{v}_\perp) = \sum_{i=1}^{4} n_i \boldsymbol{\varepsilon}_i = \sum_{i=1}^{4} n_i (\mathbf{e}_i,\mathbf{e}_{i_\perp}) \tag{39}$$

In this way, the lift of any square-triangle tiling is a subset off the 4D periodic lattice with the basis $\{\boldsymbol{\varepsilon}_1,\boldsymbol{\varepsilon}_2,\boldsymbol{\varepsilon}_3,\boldsymbol{\varepsilon}_4\}$. It is worth noting that this 4D lattice is not cubic (for instance, all vectors $\boldsymbol{\varepsilon}_i$ have the norm $a\sqrt{2}$ and the volume of the unit cell is $3a^2$). Instead, this lattice can be considered as a direct sum of regular triangular lattices belonging to two orthogonal 2D-planes in the space $P\oplus P_\perp$, which we denote by $P_{T_{13}}$ and $P_{T_{24}}$. The 2D-plane

$P_{T_{13}}$ is defined by the two 4D vectors $\boldsymbol{\varepsilon}_1$ and $\boldsymbol{\varepsilon}_3$, with vertices $(\mathbf{v},\mathbf{v}_\perp) = n_1\boldsymbol{\varepsilon}_1 + n_3\boldsymbol{\varepsilon}_3$. Similarly, the two lattice vectors $\boldsymbol{\varepsilon}_2$ and $\boldsymbol{\varepsilon}_4$ define the 2D-plane $P_{T_{24}}$. In Fig. 19, a scheme illustrates these relationships, underlining the fact that the two 2D-planes $P_{T_{13}}$ and $P_{T_{24}}$ are orthogonal to each other, but not to P and $P_\perp$.

The coordinates of the 4D-vectors $\{\boldsymbol{\varepsilon}_1,\boldsymbol{\varepsilon}_2,\boldsymbol{\varepsilon}_3,\boldsymbol{\varepsilon}_4\}$ in the $(\mathbf{I},\mathbf{J},\mathbf{K},\mathbf{L})$ orthonormal basis introduced previously (see A.1) reads:

$$(\boldsymbol{\varepsilon}_1,\boldsymbol{\varepsilon}_2,\boldsymbol{\varepsilon}_3,\boldsymbol{\varepsilon}_4) = a\left(\begin{pmatrix}1\\0\\1\\0\end{pmatrix},\begin{pmatrix}\sqrt{3}/2\\1/2\\-\sqrt{3}/2\\-1/2\end{pmatrix},\begin{pmatrix}1/2\\\sqrt{3}/2\\1/2\\\sqrt{3}/2\end{pmatrix},\begin{pmatrix}0\\1\\0\\-1\end{pmatrix}\right) \quad (40)$$

As $\boldsymbol{\varepsilon}_i = (\mathbf{e}_i,\mathbf{e}_{i_\perp})$, the two first coordinates of $\boldsymbol{\varepsilon}_i$ in the orthonormal

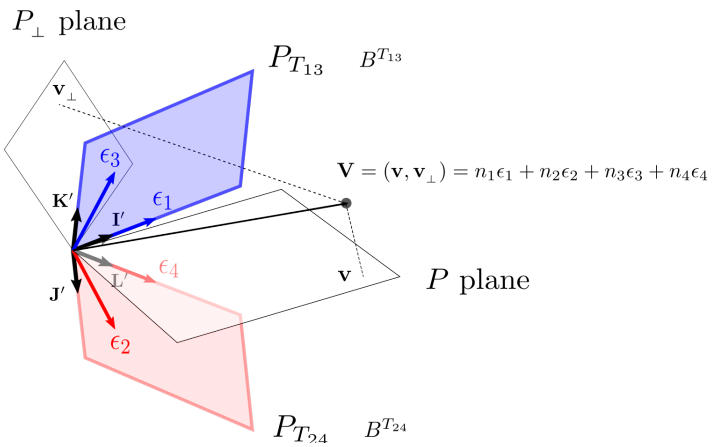

Fig. 19 Scheme of the 4D periodic lattice of basis vectors $\{\boldsymbol{\varepsilon}_1,\boldsymbol{\varepsilon}_2,\boldsymbol{\varepsilon}_3,\boldsymbol{\varepsilon}_4\}$.

basis $(\mathbf{I},\mathbf{J},\mathbf{K},\mathbf{L})$ are the coordinates of $\mathbf{e}_i$ in P (see Eq. 1) when the two last ones are the coordinates of $\mathbf{e}_{i_\perp}$ in $P_\perp$ (see Eq. 38).

In the second orthonormal basis $(\mathbf{I}',\mathbf{J}',\mathbf{K}',\mathbf{L}')$ introduced in A.1 (see Eq. 35), the basis vectors of the 4D periodic lattice read:

$$\begin{aligned}
\boldsymbol{\varepsilon}_1 &= a\sqrt{2}\mathbf{I}'\\
\boldsymbol{\varepsilon}_2 &= a\sqrt{2}(\frac{\sqrt{3}}{2}\mathbf{J}' + \frac{1}{2}\mathbf{L}')\\
\boldsymbol{\varepsilon}_3 &= a\sqrt{2}(\frac{1}{2}\mathbf{I}' + \frac{\sqrt{3}}{2}\mathbf{K}')\\
\boldsymbol{\varepsilon}_4 &= a\sqrt{2}\mathbf{L}'
\end{aligned} \quad (41)$$

$$(\boldsymbol{\varepsilon}_1,\boldsymbol{\varepsilon}_2,\boldsymbol{\varepsilon}_3,\boldsymbol{\varepsilon}_4)_{\mathbf{I}'\mathbf{J}'\mathbf{K}'\mathbf{L}'} = a\sqrt{2}\left(\begin{pmatrix}1\\0\\0\\0\end{pmatrix},\begin{pmatrix}0\\\sqrt{3}/2\\0\\1/2\end{pmatrix},\begin{pmatrix}1/2\\0\\\sqrt{3}/2\\0\end{pmatrix},\begin{pmatrix}0\\0\\0\\1\end{pmatrix}\right) \quad (42)$$

The fact that the 2D-planes $P_{T_{13}}$ and $P_{T_{24}}$ are orthogonal to each other is obtained here as they identify respectively to $(\mathbf{I}',\mathbf{K}')$ and $(\mathbf{J}',\mathbf{L}')$, two mutually orthogonal 2D-planes generated by basis vectors of the second orthonormal basis. Morover, in Eq. 42, the direct sum into two triangular lattices is more obvious than in Eq. 40.

A.3 4D reciprocal lattice for diffraction

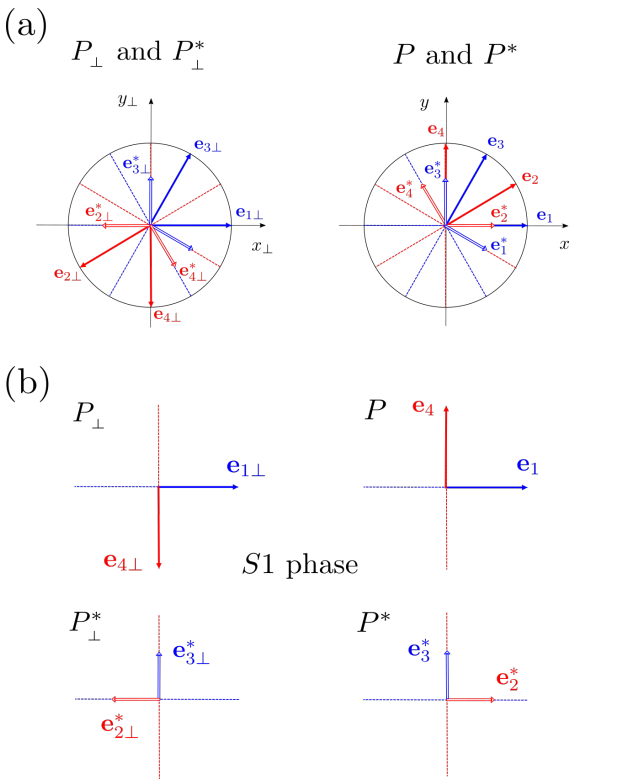

Fig. 20 Reciprocal lattice in 4D. (a) Lattice vectors and associated reciprocal lattice vectors. P^* and $P^*_\perp$ are the reciprocal planes associated to P and $P_\perp$. (b) Illustration for the pure phase $S1$ made of square tiles generated by the lattice vectors $\mathbf{e}_1$ and $\mathbf{e}_4$ in the plane P.

The 4D reciprocal lattice is defined by generalising the usual definitions in 3D :

$$\boldsymbol{\varepsilon}_i\boldsymbol{\varepsilon}^*_j = 2\pi\delta_{ij} \quad (43)$$

It leads to the following reciprocal lattice 4D-vectors, expressed in the second orthonormal basis $(\mathbf{I}',\mathbf{J}',\mathbf{K}',\mathbf{L}')$ (see Eq. 35) :

$$\begin{aligned}
\boldsymbol{\varepsilon}^*_1 &= \frac{2\pi}{a\sqrt{2}}\frac{2}{\sqrt{3}}(\frac{\sqrt{3}}{2}\mathbf{I}' - \frac{1}{2}\mathbf{K}')\\
\boldsymbol{\varepsilon}^*_2 &= \frac{2\pi}{a\sqrt{2}}\frac{2}{\sqrt{3}}\mathbf{J}'\\
\boldsymbol{\varepsilon}^*_3 &= \frac{2\pi}{a\sqrt{2}}\frac{2}{\sqrt{3}}\mathbf{K}'\\
\boldsymbol{\varepsilon}^*_4 &= \frac{2\pi}{a\sqrt{2}}\frac{2}{\sqrt{3}}(-\frac{1}{2}\mathbf{J}' + \frac{\sqrt{3}}{2}\mathbf{L}')
\end{aligned} \quad (44)$$

The reciprocal 4D-vectors in the orthonormal basis $(\mathbf{I},\mathbf{J},\mathbf{K},\mathbf{L})$ read:

$$(\boldsymbol{\varepsilon}_1^*,\boldsymbol{\varepsilon}_2^*,\boldsymbol{\varepsilon}_3^*,\boldsymbol{\varepsilon}_4^*)=\frac{2\pi}{a\sqrt{3}}\left(\begin{pmatrix}\sqrt{3}/2\\-1/2\\\sqrt{3}/2\\-1/2\end{pmatrix},\begin{pmatrix}1\\0\\-1\\0\end{pmatrix},\begin{pmatrix}0\\1\\0\\1\end{pmatrix},\begin{pmatrix}-1/2\\\sqrt{3}/2\\1/2\\-\sqrt{3}/2\end{pmatrix}\right) \tag{45}$$

The associated 2D lattice vectors in P^* and $P_\perp^*$ are labelled respectively $(\boldsymbol{e}_1^*,\boldsymbol{e}_2^*,\boldsymbol{e}_3^*,\boldsymbol{e}_4^*)$ and $(\boldsymbol{e}_{1\perp}^*,\boldsymbol{e}_{2\perp}^*,\boldsymbol{e}_{3\perp}^*,\boldsymbol{e}_{4\perp}^*)$. They are plotted in Figure 20.

B Global uniformity

For the proof of proposition 1 (section 4.2), let us start by proving the "if" statement. Consider an infinite square-triangle tiling with an asymptotically linear lifting map of the form (16) and a sequence of growing patches $(\mathscr{P}_i)$ (see Figure 4) such that the ratio $|\partial\mathscr{P}_i|^2/|\mathscr{P}_i|$ is bounded. Let $J(\mathbf{x})$ stand for the Jacobian derivative of φ:

$$J_{\alpha\beta}(\mathbf{x})=\frac{\partial\varphi_\alpha(\mathbf{x})}{\partial x^\beta},$$

where the point $\mathbf{x}\in\mathscr{P}_i$ lies in the interior of a tile. This 2×2 matrix-valued function takes five possible values given by the matrices B_Φ from Table 2. Notably, $\det(J(\mathbf{x}))$ equals 1 if $\mathbf{x}$ is inside a triangle and -1 for $\mathbf{x}$ lying inside a square. Therefore, the area-weighted average of $\det(J(\mathbf{x}))$ over $\mathscr{P}_i$ is given by the formula

$$\langle\det(J(\mathbf{x}))\rangle_{\mathscr{P}_i}=|\mathscr{P}_i|^{-1}\int_{\mathscr{P}_i}\det(J(\mathbf{x}))\,\mathrm{d}\mathbf{x}=\tau(\mathscr{P}_i)-\sigma(\mathscr{P}_i). \tag{46}$$

By Stokes' theorem, one can express the integral over the patch $\mathscr{P}_i$ in (46) via an integral over its boundary $\partial\mathscr{P}_i$:

$$\int_{\mathscr{P}_i}\det(J(\mathbf{x}))\,\mathrm{d}\mathbf{x}=\int_{\mathscr{P}_i}\mathrm{d}\varphi(\mathbf{x})\wedge\mathrm{d}\varphi(\mathbf{x})=\frac{1}{2}\varepsilon^{\alpha\beta}\oint_{\partial\mathscr{P}_i}\varphi_\alpha(\mathbf{x})\,\mathrm{d}\varphi_\beta(\mathbf{x}), \tag{47}$$

where $\varepsilon^{\alpha\beta}$ is the Levi-Civita symbol and the integration over $\partial\mathscr{P}_i$ is performed counterclockwise. Since one can always choose the origin of the coordinate system within the patch $\mathscr{P}_i$, we can safely assume that $\|\mathbf{x}\|<|\partial\mathscr{P}_i|$ for all points in the path of the integral in (47). Then, equation (16) gives rise to the following asymptotic formula:

$$\oint_{\partial\mathscr{P}_i}\varphi_\alpha(\mathbf{x})\mathrm{d}\varphi_\beta(\mathbf{x})=B_{\alpha\gamma}\oint_{\partial\mathscr{P}_i}x^\gamma\mathrm{d}\varphi_\beta(\mathbf{x})+o(|\partial\mathscr{P}_i|^2). \tag{48}$$

The asymptotic behavior of the integral in (48) can be obtained in the same way:

$$\oint_{\partial\mathscr{P}_i}x^\gamma\,\mathrm{d}\varphi_\beta(\mathbf{x})=-\oint_{\partial\mathscr{P}_i}\varphi_\beta(\mathbf{x})\,\mathrm{d}x^\gamma=-B_{\beta\delta}\oint_{\partial\mathscr{P}_i}x^\delta\,\mathrm{d}x^\gamma+o(|\partial\mathscr{P}_i|^2). \tag{49}$$

By combining equations (46), (47), (48) and (49), and taking into account the following identities:

$$\oint_{\partial\mathscr{P}_i}x^\delta\,\mathrm{d}x^\gamma=\varepsilon^{\delta\gamma}|\mathscr{P}_i|$$

$$-\frac{1}{2}\varepsilon^{\alpha\beta}\varepsilon^{\delta\gamma}B_{\alpha\gamma}B_{\beta\delta}=\det(B),$$

we obtain

$$\tau(\mathscr{P}_i)-\sigma(\mathscr{P}_i)=\det(B)+o\left(|\partial\mathscr{P}_i|^2\right)/|\mathscr{P}_i|. \tag{50}$$

Consider now the area-weighted average of $J(\mathbf{x})$ over the patch $\mathscr{P}_i$:

$$\langle J_{\alpha\beta}\rangle_{\mathscr{P}_i}=\frac{1}{|\mathscr{P}_i|}\int_{\mathscr{P}_i}J_{\alpha\beta}(\mathbf{x})\,\mathrm{d}^2\mathbf{x}. \tag{51}$$

Again, using Stokes' theorem we get

$$\langle J_{\alpha\beta}\rangle_{\mathscr{P}_i}=\frac{\varepsilon_{\beta\gamma}}{2|\mathscr{P}_i|}\oint_{\partial\mathscr{P}_i}\varphi_\alpha(\mathbf{x})\,\mathrm{d}x^\gamma$$

As follows from equation (16), the above integral behaves asymptotically as

$$\oint_{\partial\mathscr{P}_i}\varphi_\alpha(\mathbf{x})\,\mathrm{d}x^\gamma=B_{\alpha\delta}\oint_{\partial\mathscr{P}_i}x^\delta\,\mathrm{d}x^\gamma+o(|\partial\mathscr{P}_i|^2)=B_{\alpha\delta}\varepsilon^{\delta\gamma}|\mathscr{P}_i|+o(|\partial\mathscr{P}_i|^2).$$

This gives rise to the following estimate of $\langle J\rangle_{\mathscr{P}_i}$:

$$\langle J_{\alpha\beta}\rangle_{\mathscr{P}_i}=B_{\alpha\beta}+o\left(|\partial\mathscr{P}_i|^2\right)/|\mathscr{P}_i|. \tag{52}$$

The integral in (51) can also be computed as a sum of contributions of individual tile species, yielding

$$\langle J\rangle_{\mathscr{P}_i}=\sigma_1(\mathscr{P}_i)B^{S1}+\sigma_2(\mathscr{P}_i)B^{S2}+\sigma_3(\mathscr{P}_i)B^{S3}+ \\ +\tau_{13}(\mathscr{P}_i)B^{T13}+\tau_{24}(\mathscr{P}_i)B^{T24}, \tag{53}$$

where the matrices B^{S1}, B^{S2}, B^{S3}, B^{T13} and B^{T24} are given in Table 2. Since these matrices are symmetric, this equation contains three linear constraints on the area fractions of different tile species in $\mathscr{P}_i$. Together with (46) and the condition

$$\sigma_1(\mathscr{P}_i)+\sigma_2(\mathscr{P}_i)+\sigma_3(\mathscr{P}_i)+\tau_{13}(\mathscr{P}_i)+\tau_{24}(\mathscr{P}_i)=1$$

these constraints fix entirely the area fractions in terms of $\langle J_{\alpha\beta}\rangle_{\mathscr{P}_i}$ and $\langle\det(J(\mathbf{x}))\rangle_{\mathscr{P}_i}$. On the other hand, since $|\partial\mathscr{P}_i|^2/|\mathscr{P}_i|$ is assumed bounded, equations (52) and (50) read as

$$\lim_{i\to\infty}\langle J_{\alpha\beta}\rangle_{\mathscr{P}_i}=B_{\alpha\beta}$$

and

$$\lim_{i\to\infty}\langle\det(J(\mathbf{x}))\rangle_{\mathscr{P}_i}=\det(B).$$

Therefore, the area fractions $\sigma_1(\mathscr{P}_i)$, $\sigma_2(\mathscr{P}_i)$, $\sigma_3(\mathscr{P}_i)$, $\tau_{13}(\mathscr{P}_i)$ and $\tau_{24}(\mathscr{P}_i)$ have well-defined limits (see eq. (3)) and the considered tiling is globally uniform.

Let us now prove the "only if" part of Proposition 1. We shall proceed by *reductio ad absurdum*. Let us assume that there exists a globally uniform tiling such that its lifting map φ is not asymptotically linear. For a globally uniform tiling one can define the matrix B by the formula

$$B_{\alpha\beta}=\lim_{|\mathscr{P}_i|\to\infty}\langle J_{\alpha\beta}\rangle_{\mathscr{P}_i}, \tag{54}$$

for any sequence of patches $\mathscr{P}_i$, such that the ratio $|\partial\mathscr{P}_i|^2/|\mathscr{P}_i|$ is bounded. By the hypothesis, there should exist a real constant $M>0$ such that one can a vector $\mathbf{x}\in P$ of an arbitrarily large norm $l=\|\mathbf{x}\|$ for which

$$\|\varphi(\mathbf{x})-B\cdot\mathbf{x}\|>Ml. \tag{55}$$

Let us consider a rectangle $\mathscr{R}\subset P$ of dimensions $l\times\frac{Ml}{2}$ such that

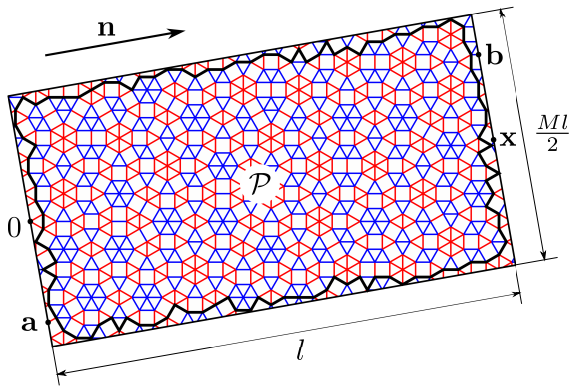

Fig. 21 The rectangular region $\mathscr{R}$ used in the proof of Proposition 1. The bold broken line is the boundary of the largest tiling patch $\mathscr{P}$ contained withing $\mathscr{R}$.

the points 0 and $\mathbf{x}$ are the centers of its edges of length $\frac{Ml}{2}$ (see Figure 21). Denote by n^β the components of the unit vector $\mathbf{n} = \mathbf{x}/\|\mathbf{x}\|$. By Stoke's theorem, we get

$$n^\beta \left(\langle J_{\alpha\beta} \rangle_{\mathscr{R}} - B_{\alpha\beta} \right) = \frac{n^\beta \varepsilon_{\beta\gamma}}{Ml^2} \oint_{\partial\mathscr{R}} \left(\varphi_\alpha(\mathbf{x}) - B_{\alpha\delta} x^\delta \right) \mathrm{d}x^\gamma \qquad (56)$$

The contribution of the edges of $\mathscr{R}$ parallel to $\mathbf{x}$ to the right-hand side of (56) vanishes after multiplication by $n^\beta \varepsilon_{\beta\gamma}$. To estimate the contribution of the remaining two edges, we observe that the integrand in (56) is Lipschitz continuous with Lipschitz constant 2. Indeed, the spectral radius of the Jacobian derivative J (and hence also that of the matrix B in (54)) is bounded by 1. Therefore, taking into account (55), for any two points $\mathbf{a}$ and $\mathbf{b}$ belonging respectively to the edges of $\mathscr{R}$ containing 0 and $\mathbf{x}$ (see Figure 21), one has

$$\begin{aligned} \|\varphi(\mathbf{a}) - B\cdot\mathbf{a}\| &\le 2\|\mathbf{a}\| \\ \|\varphi(\mathbf{b}) - B\cdot\mathbf{b}\| &\ge Ml - 2\|\mathbf{b}-\mathbf{x}\| \end{aligned} \qquad (57)$$

Formulas (57) provide a lower bound for the integral in (56), giving rise to the following inequality

$$\| (\langle J \rangle_{\mathscr{R}} - B)\cdot\mathbf{n} \| \ge \frac{M}{4}.$$

Let now $\mathscr{P}$ stand for the largest patch of the tiling contained within the rectangle $\mathscr{R}$. As the aspect ratio of $\mathscr{R}$ is fixed, $|\partial\mathscr{P}|^2/|\mathscr{P}|$ is bounded from above by some constant not depending on l. For large l, the contribution of the interstice between $\mathscr{P}$ and $\mathscr{R}$ to $\langle J \rangle_{\mathscr{P}}$ is negligible and one has

$$\| (\langle J \rangle_{\mathscr{P}} - B)\cdot\mathbf{n} \| \ge \frac{M}{4} + o(1) \qquad \text{as } l \to \infty. \qquad (58)$$

Since by the assumption the norm of $\mathbf{x}$ can be arbitrarily large, we can construct a sequence of patches $\mathscr{P}_i$, such that the ratio $|\partial\mathscr{P}_i|^2/|\mathscr{P}_i|$ is bounded from above, but $\| \langle J \rangle_{\mathscr{P}_i} - B \|$ is bounded from below, in contradiction with (54). This contradiction proves the statement.

As now the equivalence between the global uniformity and the asymptotic linearity of the lifting map is established, to finish the proof it remains only to observe that (53) in the limit of infinite tilings gives

$$B = \sigma_1 B^{S1} + \sigma_2 B^{S2} + \sigma_3 B^{S3} + \tau_{13} B^{T13} + \tau_{24} B^{T24}. \qquad (59)$$

yielding (17). Similarly, the equation (18) arises as the limit of (46).

C Special phases

C.1 The Σ phase

C.1.1 Structure factor of the Σ phase

The 3^2434 vertices have four different orientations depicted in black, blue, magenta and green in the different figures. The edge's size of the centered square unit cell is $a_\Sigma = a(1+\sqrt{3})$ where a is the edge's size of the tiles. It contains eight vertices when the square primitive unit cell contains four vertices. As pictured in Figure 9, each set of vertices having the same color forms a regular square lattice of edge's size $a(1+\sqrt{3})/\sqrt{2}$, turned by an angle of $\pi/4$ with respect to the centered square unit cell. Starting from one of these four regular square lattices, the three other ones can be obtained by translation using the three translation vectors $\mathbf{e}_1$, $\mathbf{e}_3$ and $\mathbf{e}_1 - \mathbf{e}_3$.

The 2D structure factor of the Σ phase is defined as the Fourier

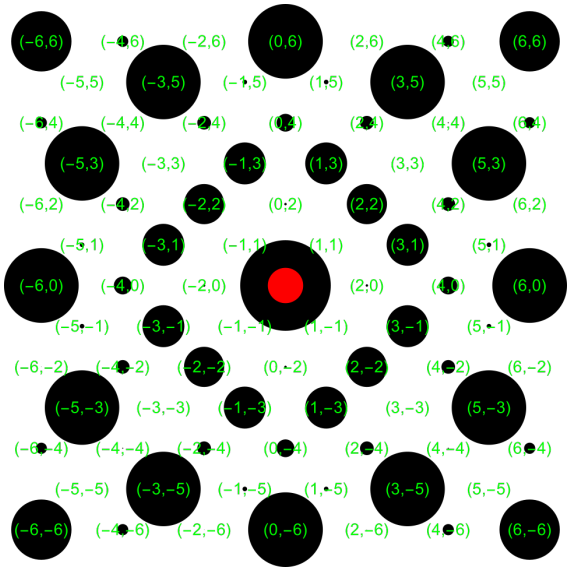

Fig. 22 Detail of the structure factor of the Σ phase including HK indices (see also Figure 10). The twelvefold symmetry is only approximate. The (60) and (53) peaks are not exactly positioned on the same circle ($G^*_{53}/G^*_{60} = 0.9718$) and their intensities are not exactly the same ($I_{53}/I_{60} = 0.9976$).

transform of the points lattice located on the vertices. It can be calculated taking for example the following coordinates of the four vertices in the plane P (using unit vectors $\frac{1}{a}\mathbf{e}_1$ and $\frac{1}{a}\mathbf{e}_4$):

$$(a/2,0)\ (-a/2,0)\ \left(0, a\sqrt{3}/2\right)\ \left(0, -a\sqrt{3}/2\right)$$

The 2D structure factor consists in a periodic lattice of diffraction peaks that can be indexed using two integer indices HK

$$\mathbf{G}^*_{HK} = \frac{2\pi}{a_\Sigma}\left(H\frac{1}{a}\mathbf{e}_1 + K\frac{1}{a}\mathbf{e}_4\right) = \frac{2\pi}{a\left(1+\sqrt{3}\right)}\left(H\frac{1}{a}\mathbf{e}_1 + K\frac{1}{a}\mathbf{e}_4\right) \tag{60}$$

and the intensities of the Bragg peaks are $I_{HK} = |F_{HK}|^2$ with:

$$F_{HK} = 2\left[1+(-1)^{(H+K)}\right]\left[\cos\left(\frac{\pi}{1+\sqrt{3}}H\right) + \cos\left(\frac{\pi\sqrt{3}}{1+\sqrt{3}}K\right)\right] \tag{61}$$

The 2D structure factor is shown in Figures 10 and 22. A remarkable feature is that the modulations in the intensities are not periodic, as can be seen in the expression of F_{HK} in the cosine terms due to the presence of irrational terms. This is due to the irrational coordinates of the lattice points in the square unit cell. This feature of the structure factor is linked to the intrinsic incommensurability of square-triangle tilings.

In Figure 22, the HK indices are reported for some Bragg peaks. The set of twelve diffraction peaks with $(6,0)$ and $(5,3)$ indices is remarkable as it form an approximate figure with 12-fold symmetry. But it is only approximate as the peaks are not exactly positioned all on the same circle ($G^*_{53}/G^*_{60} = 0.9718$) and their intensities are not exactly the same ($I_{53}/I_{60} = 0.9976$), with tiny differences of less than 1 percent.

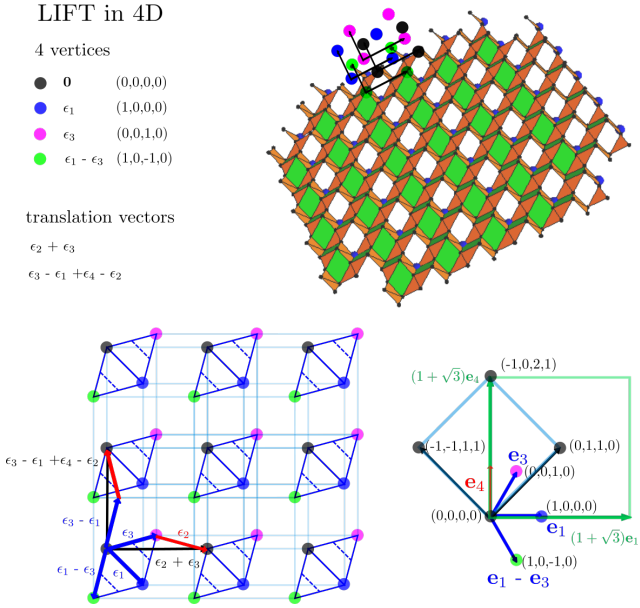

Fig. 23 Lift in 4D of the Σ phase. The 4D vertices are located in four different 2D-planes having the same hyperslope B^Σ and which are translated from each other. In each 2D-plane, the vertices have the same orientation (same color) and form a regular square lattice.

C.1.2 4D lift of the Σ phase

The lift construction in the 4D space consists in associating to each vertex in the plane P a 4D lifted vertex. This association can be done in different ways. Here we choose to place the origin of the plane P on a black vertex which is lifted to the origin of the 4D space (see Figure 23). A blue vertex near to the origin is lifted to the 4D vertex $\boldsymbol{\epsilon}_1$, a magenta one to $\boldsymbol{\epsilon}_3$ and a green one to $\boldsymbol{\epsilon}_1 - \boldsymbol{\epsilon}_3$. In 4D, all other vertices are obtained by translation. All vertices of the same color are lifted in the same 2D-plane using the two translation vectors $\boldsymbol{\epsilon}_2 + \boldsymbol{\epsilon}_3$ and $\boldsymbol{\epsilon}_3 - \boldsymbol{\epsilon}_1 + \boldsymbol{\epsilon}_4 - \boldsymbol{\epsilon}_2$. The black vertices are embedded in a plane containing the origin when the three other planes are parallel to this plane and can be deduced by translation from the origin using $\boldsymbol{\epsilon}_1$ (blue vertices), $\boldsymbol{\epsilon}_3$ (magenta vertices) and $\boldsymbol{\epsilon}_1 - \boldsymbol{\epsilon}_3$ (green vertices).

The expression of the matrix B^Σ is given in Eq. 20. Its expression can be identified to the hyperslope with respect to the plane P (2x2 matrix A, see Eq. 34) of the plane defined by the two vectors $\boldsymbol{\epsilon}_2 + \boldsymbol{\epsilon}_3$ and $\boldsymbol{\epsilon}_3 - \boldsymbol{\epsilon}_1 + \boldsymbol{\epsilon}_4 - \boldsymbol{\epsilon}_2$. It can be verified from the expression of the $(\boldsymbol{\epsilon}_1, \boldsymbol{\epsilon}_2, \boldsymbol{\epsilon}_3, \boldsymbol{\epsilon}_4)$ 4D-vectors in the $(\mathbf{I}, \mathbf{J}, \mathbf{K}, \mathbf{L})$ orthonormal basis (see Eq. 40), leading to:

$$\boldsymbol{\epsilon}_2 + \boldsymbol{\epsilon}_3 = a\begin{pmatrix}\alpha\\ \alpha\\ -\beta\\ \beta\end{pmatrix}; \boldsymbol{\epsilon}_3 - \boldsymbol{\epsilon}_1 + \boldsymbol{\epsilon}_4 - \boldsymbol{\epsilon}_2 = a\begin{pmatrix}-\alpha\\ \alpha\\ \beta\\ \beta\end{pmatrix} \tag{62}$$

with

$$\alpha = (\sqrt{3}+1)/2; \beta = (\sqrt{3}-1)/2 \tag{63}$$

Using the general expression of the hyperslope (2x2 matrix A) with respect to the plane P (see Eq. 34), the identity $A = B^\Sigma$ is verified.

To construct the projections in the planes P and $P_\perp$ (see Figure 9), we use the four integer indices notation already introduced in equation 39. The lift construction allows to index each vertex with a unique set of four integers (n_1, n_2, n_3, n_4) writing that $(\mathbf{v}, \mathbf{v}_\perp) = n_1\boldsymbol{\epsilon}_1 + n_2\boldsymbol{\epsilon}_2 + n_3\boldsymbol{\epsilon}_3 + n_4\boldsymbol{\epsilon}_4$. For example, the black 4D vertices have the following 4D integer coordinates where n, m are two integers:

$$(\mathbf{v}, \mathbf{v}_\perp)_{\text{black}} = n(\boldsymbol{\epsilon}_2 + \boldsymbol{\epsilon}_3) + m(\boldsymbol{\epsilon}_3 - \boldsymbol{\epsilon}_1 + \boldsymbol{\epsilon}_4 - \boldsymbol{\epsilon}_2) = \begin{pmatrix}-m\\ n-m\\ n+m\\ m\end{pmatrix} \tag{64}$$

C.1.3 Infinite sequence of phases with the same composition.

To illustrate the fact that, except for the five pure phases, any composition point corresponds to an infinite number of phases, let's consider the following transformation (Figure 24).

It consists in replacing each triangle and square by four identical tiles and applying afterwards a scale factor of two to keep the tile's dimension. This transformation preserves both the ratio N_t/N_s and the tiles orientation distribution so the 3D composition point is fixed. By applying it several times, one can generate an infinite sequence of other phases located at the same composition point. Applied at a composition point like $\boldsymbol{\Sigma}_1$, starting from the Σ phase, an infinite sequence of periodic phases with increasing unit cell size is obtained. Note that all these periodic phases are globally uniform and couldn't be generated by a cut-and-project method. The infinite limit is a coexistence of domains of four pure phases around a junction point (see section 6.2).

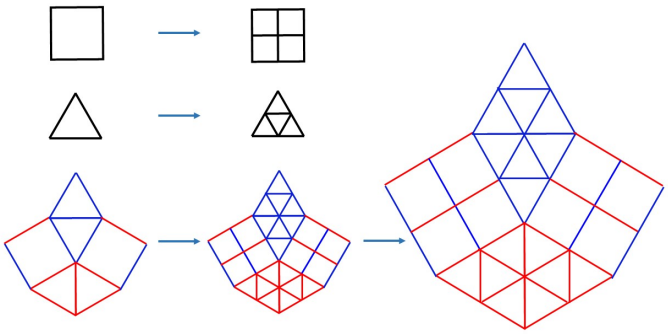

Fig. 24 A simple transformation of tiles generating an infinite sequence of phases at a fixed composition point. The ratio N_t/N_s is preserved as both tiles number are multiplied by a factor four and the tiles orientation distribution is the same as well. It is illustrated at the composition point $\mathbf{\Sigma}_1$.

C.2 Structure factor of the H phase

The 2D structure factor of the Archimedean H phase is calculated in a similar way as for the Σ phase using a rectangular centered lattice of dimensions a and $(2+\sqrt{3})a$ with two vertices per node at positions $(0,a/2)$ and $(0,-a/2)$ (see Figure 8 for the orientation of the H phase). The 2D structure factor is shown in Figure 25 and consists in a periodic set of Bragg peaks that can be indexed by two integer indices HK of intensities $I_{HK}=|F_{HK}|^2$ with:

$$F_{HK}=2\left[1+(-1)^{(H+K)}\right]cos\left(\frac{\pi K}{2+\sqrt{3}}\right) \tag{65}$$

A remarkable feature is the way how the intensities of the

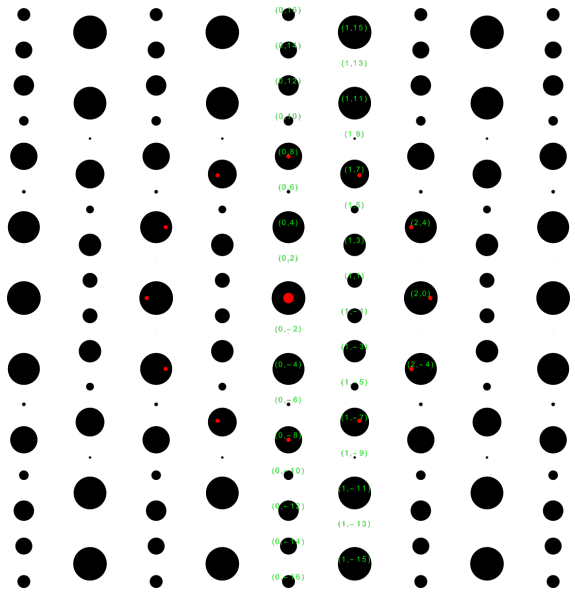

Fig. 25 Structure factor of the H phase. The infinite 1D stripes are horizontal and the stack direction is vertical like in Figure 8.

Bragg peaks are modulated. The whole structure factor can be decomposed in two types of infinite vertical lines of Bragg peaks of intensities I_{0K} with K even and I_{1K} with K odd. Along the horizontal direction, these lines of Bragg peaks alternate in a simple periodic fashion. This is expected because the infinite stripes of tiles along the horizontal direction are periodic (rows of square or triangles) (see Figure 8). But along the vertical direction, the intensities are modulated via the cosine term in eq. 65. Because of the presence of the irrational ratio $2+\sqrt{3}$, it is impossible for two diffraction peaks to have exactly the same intensity. In other words, even if the cosine function is periodic, it is sampled at irrational values. It comes from the fact the period of the 1D stack of stripes, here $(2+\sqrt{3})a$, is incommensurate with a.

This aperiodicity in the Bragg peak intensities along the stack direction is a strong signature of the incommesurability between the two tiles dimensions, a and $a\sqrt{3}/2$. In a system where the two tiles dimensions would be in a rational ratio, in the cosine term, this ratio would appear as a fraction of two integers, and the Bragg peaks intensities would exhibit periodic modulations along the stack direction.

One can also notice in Figure 25 that a set of twelve diffraction peaks show an approximate 12-fold symmetry, but this feature is much less striking than for the Σ phase (see Figures 10 and 22). It makes sense as the 3D composition point of the H phase is very asymmetric.

C.3 Striped phases

C.3.1 Stacking sequence and average slope

The stacking sequence is built using two vectors, $\mathbf{e}_4$ for square tiles and $\mathbf{e}_3$ for the triangular tiles. The vertices in plane P have the form $\mathbf{v}=n_1\mathbf{e}_1+n_3\mathbf{e}_3+n_4\mathbf{e}_4$, with the stripes direction along $\mathbf{e}_1$. The stack of the stripes is given by a sequence of vectors $\mathbf{e}_3$ (stripe of triangular tiles) and $\mathbf{e}_4$ (stripe of square tiles) that follows a straight line which slope $b(\tau)$ is related to the composition, as illustrated in Figure 11a. Simultaneously in $P_\perp$, the associated vertices are $\mathbf{v}_\perp=n_1\mathbf{e}_{1_\perp}+n_3\mathbf{e}_{3_\perp}+n_4\mathbf{e}_{4_\perp}$. As a result, in the plane P, the stacking sequence ($\mathbf{e}_3$ and $\mathbf{e}_4$ lattice vectors) follows a straight line of slope $b(\tau)$. Similarly, in the plane $P_\perp$, the stacking sequence (made of $\mathbf{e}_{3_\perp}$ and $\mathbf{e}_{4_\perp}$ lattice vectors) follows a straight line of slope $b_\perp(\tau)$. The expression of these two slopes read:

$$b(\tau)=\frac{y}{x}=\frac{\sqrt{3}}{\tau},$$

$$b_\perp(\tau)=\frac{y_\perp}{x_\perp}=\sqrt{3}\frac{\tau-\sigma}{\tau}=\sqrt{3}\frac{2\tau-1}{\tau} \tag{66}$$

If only square tiles are present ($\tau=0$), the average slope in the plane P is vertical and the striped phase is the $\mathbf{S}_1$ pure phase (see Figure 11a). Similarly, for $\tau=1$, the slope coefficient is equal to $\sqrt{3}$ and the striped phase is the $\mathbf{T}_{13}$ pure phase. For all other compositions, the average slope is in between these two values. In particular, for $\tau=\frac{1}{2}$, $b=2\sqrt{3}$ (plane P) and $b_\perp=0$ (plane $P_\perp$). This last feature is characteristic of aperiodic order: the stacking sequence in the plane $P_\perp$ follows the horizontal line along $x_\perp$.

C.3.2 Staircase

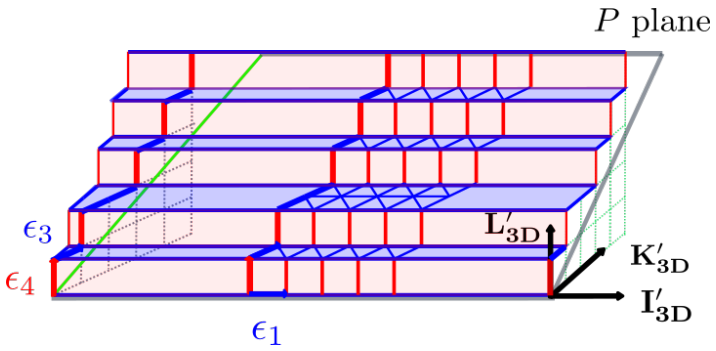

Fig. 26 Lift construction for striped phases. A stacking sequence can be visualized as a '3D staircase'. Each 'step' of the 3D staircase has a vertical side of height $a\sqrt{2}$ and an horizontal side of width $a\sqrt{2}\frac{\sqrt{3}}{2}$. Vertical portions (in red) correspond to the $\mathbf{S}_1$ pure phase when horizontal ones (in blue) correspond to the $\mathbf{T}_{13}$ pure phase. The plane defined by the two vectors ($\boldsymbol{\varepsilon}_3$, $\boldsymbol{\varepsilon}_4$) forms a square lattice of parameter $a\sqrt{2}$ and its intersection with the plane P is a line depicted in light green color.

For striped phases, the lift construction in the 4D space is made using only three vectors $(\boldsymbol{\varepsilon}_1, \boldsymbol{\varepsilon}_3, \boldsymbol{\varepsilon}_4)$ instead of 4 in the general case. The stacking sequence is expressed onto the two 4D lattice vectors $\boldsymbol{\varepsilon}_3$ and $\boldsymbol{\varepsilon}_4$. The lifted version of a striped phase can be visualised as a "staircase' (Figure 26). To do so, one can define a 3D subspace of the 4D space by taking all components along $\mathbf{J}'$ equal to zero. In this 3D subspace, all vectors have three components in an orthonormal basis $(\mathbf{I'_{3D}}, \mathbf{K'_{3D}}, \mathbf{L'_{3D}})$ which is derived from the second 4D orthonormal basis (Eq. 42) and the lattice vectors read:

$$\boldsymbol{\varepsilon}_{1,3D} = a\sqrt{2}\mathbf{I'_{3D}}$$

$$\boldsymbol{\varepsilon}_{3,3D} = a\sqrt{2}(\frac{1}{2}\mathbf{I'_{3D}} + \frac{\sqrt{3}}{2}\mathbf{K'_{3D}})$$

$$\boldsymbol{\varepsilon}_{4,3D} = a\sqrt{2}\mathbf{L'_{3D}}$$

$$(\boldsymbol{\varepsilon}_{1,3D}, \boldsymbol{\varepsilon}_{3,3D}, \boldsymbol{\varepsilon}_{4,3D})_{\mathbf{I'_{3D}}\mathbf{K'_{3D}}\mathbf{L'_{3D}}} = a\sqrt{2}\left(\begin{pmatrix}1\\0\\0\end{pmatrix}, \begin{pmatrix}1/2\\\sqrt{3}/2\\0\end{pmatrix}, \begin{pmatrix}0\\0\\1\end{pmatrix}\right) \tag{67}$$

The steps of the '3D-staircase' (see Figure 26) are along $\mathbf{L'_{3D}}$ (with a vertical edge of height $a\sqrt{2}$) and along $\mathbf{K'_{3D}}$ with a width $a\sqrt{2}\frac{\sqrt{3}}{2}$, corresponding to the coordinate of $\boldsymbol{\varepsilon}_{3,3D}$ along $\mathbf{K'_{3D}}$. Embedded in this 3D subspace, the plane P is constructed with the two vectors basis ($\mathbf{I'_{3D}}$, $\mathbf{K'_{3D}} + \mathbf{L'_{3D}}$) and the plane $P_\perp$ with ($\mathbf{I'_{3D}}$, $\mathbf{K'_{3D}} - \mathbf{L'_{3D}}$). P and $P_\perp$ are still orthogonal to each other and are turned by an angle of $\pi/4$ along $\mathbf{I'_{3D}}$. The intersection between the plane P and the plane $(\boldsymbol{\varepsilon}_{3,3D}, \boldsymbol{\varepsilon}_{4,3D})$ is along the direction $(1, \sqrt{3}, \sqrt{3})$. The irrational slope $\frac{\sqrt{3}}{2}$ (see Eq. 22) is obtained writing that this direction is along the 3D-vector $2(\frac{1}{2}\mathbf{I'_{3D}} + \frac{\sqrt{3}}{2}\mathbf{K'_{3D}}) + \sqrt{3}\mathbf{L'_{3D}}$. The plane defined by the two vectors ($\boldsymbol{\varepsilon}_{3,3D}$, $\boldsymbol{\varepsilon}_{4,3D}$) form a square lattice of parameter $a\sqrt{2}$. Note that this plane is tilted by an angle of $\pi/3$ along the vertical direction $\mathbf{L'_{3D}}$, where ($\mathbf{I'_{3D}}$, $\mathbf{K'_{3D}}$, $\mathbf{L'_{3D}}$) is a 3D orthonormal basis. The plane P is inclined at an angle of $\pi/4$ along the direction $\mathbf{K'_{3D}} + \mathbf{L'_{3D}}$. The intersection of the plane P with the plane ($\boldsymbol{\varepsilon}_{3,3D}$, $\boldsymbol{\varepsilon}_{4,3D}$) is a line shown with a light green color.

D Inflation constructions

D.1 Striped phases: 1D aperiodic order

Starting from some initial "seed", a longer sequence is constructed by using the following substitution rules: 1) each stripe s is replaced by a copies of s and four stripes t and 2) each stripe t is replaced by 3 stripes s and a copies of t, where $a \geq 0$ is an integer. Upon iteration, these substitution rules generate periodic phases with bigger and bigger unit cell, and one approaches a perfect 1D quasiperiodic structure at the limit of an infinite number of iterations. An example of the first three steps of a construction corresponding to $a = 3$ is shown in Fig. 12b.

If the number of s strips, $N_s^{(i)}$, and the number of t stripes $N_t^{(i)}$ at the ith step are known, their number at the $i+1$th step can be readily found, since the substitution rules imply that

$$\mu_{i+1} = \begin{pmatrix} a & 4 \\ 3 & a \end{pmatrix} \mu_i \tag{68}$$

where $\mu_i = \{N_s^{(i)}, N_t^{(i)}\}$.[32] The maximal eigenvalue (called the Perron root) of the 2 by 2 matrix of this equation and its corresponding eigenvector provide information on, respectively, the rate of growth of the tiling, and on the relative proportion of s and t type strips. This eigenvalue is $(a + 2\sqrt{3})$, for all values of the integer parameter a, and the corresponding eigenvector is $\{\sqrt{3}/2, 1\}$. This shows that the ratio of triangles to squares tends towards the value $\sqrt{3}/2$.

D.2 Maximally symmetric phases

The initial seed is a dodecagonal wheel (see Figure 13). Its composition is maximally symmetric. It contains the same number of T1/T3 (blue color) and T2/T4 (red color) triangles ($N_{t12,0} = N_{t34,0} = 6$), and the same number for each of the three kinds of squares ($N_{s1,0} = N_{s2,0} = N_{s3,0} = 2$). For the seed, the ratio $N_{t,0}/N_{s,0} = 12/6 = 2$ has a rational value. After an infinite number of iterations tends, this ratio in tiles number reaches the irrational value $N_t/N_s = 4/\sqrt{3}$.

Initial conditions are $N_{t,0} = 12$ and $N_{s,0} = 6$. If we denote by $N_{t,i}$ and $N_{s,i}$ the number of triangles and squares at inflation step i, after the next inflation step, these numbers are given by $N_{t,i+1} = 7N_{t,i} + 3N_{s,i}$ and $N_{s,i+1} = 16N_{t,i} + 7N_{s,i}$. This is encoded in the following transfer matrix form to compute the vector $v_i = \{N_{t,i}, N_{s,i}\}$:

$$v_{i+1} = \begin{pmatrix} 7 & 3 \\ 16 & 7 \end{pmatrix} v_i \tag{69}$$

To the Perron root $(7 + 4\sqrt{3})$ of this matrix corresponds an eigenvector $\{\sqrt{3}/4, 1\}$. It is easily checked that the limiting value of the ratio of tiles is $N_t/N_s = 4/\sqrt{3}$.

To obtain the dodecagonal QC phase shown in Fig. 13a, the following rule is followed.[32] If there are a majority of blue bonds

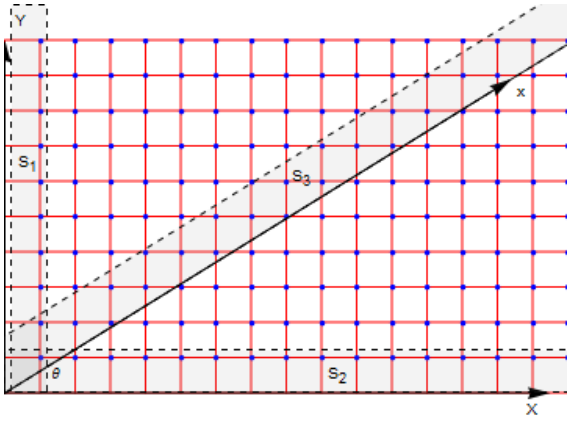

Fig. 27 Selection stripes for i) the periodic sequence of B-tiles (S_1, $\theta = \pi/2$) ii) the periodic sequence of A-tiles (S_2, $\theta = 0$) and iii) the Fibonacci quasiperiodic sequence (S_3, $\theta = \arctan(1/\lambda_1)$). Selected points are projected onto the "physical" x axis, giving rise to a sequence of A and B tiles.

emanating from the 'parent' site then the dodecagon contains a B hexagon, and otherwise it contains the R hexagon. Note that in this construction, it is impossible to get four squares around a site during the inflation process, so the rule can always be applied, in the interior of the patch. For the sites located on the border of the patch at a given iteration step, one needs to examine the environment of that after the next iteration step. This is the rule applied to obtain the patch after one inflation step.

E Diffraction

In this section we discuss some properties of the structure factor, $S(\vec{q})$, a physical quantity which is measurable by a diffraction experiment and useful to distinguish between different types of spatial organization of particles. It is defined by $VS(\vec{q}) = |\rho(\vec{q})|^2$ where V is the volume of the sample and $\rho(\vec{q})$ is the Fourier transform of the spatial density. We will consider the simplest situation in which unit point masses are located at each vertex, $\rho(\vec{r}) = \sum_j \delta(\vec{r} - \vec{R}_j)$ where $\delta(\vec{r})$ is a delta-function and $\vec{R}_j$ are the positions of the N particles $j = 1, ..., N$.

E.1 The Fibonacci sequence

To explain how one can compute the structure factor of a quasicrystal and its periodic approximants, it is convenient to begin with a one dimensional example, the Fibonacci sequence. This 1D quasicrystal is an infinite sequence built of two kinds of tiles (line segments) called A and B. This quasicrystal can be lifted to a square grid in a 2D space by using the following rules: every A tile corresponds, in 2D, to a horizontal displacement $a\vec{u}_X$, and each B tile to a vertical displacement $a\vec{u}_Y$. This results in a broken path in 2D (see Fig.27) linking vertices that lie inside a stripe having a slope equal to λ_1^{-1} where $\lambda_1 = \frac{1+\sqrt{5}}{2}$ is the golden mean. Note that the same construction can be done for any other irrational slope like $\sqrt{3}/2$ (see section 5.3). The x axis is parallel to the strip, and represents the physical direction while the y axis (not shown) is the perpendicular direction. The lengths of the A and B tiles are $x_A = a\cos\theta$ and $x_B = a\sin\theta$ respectively. The "selection strip" (so-called for evident reasons) has a width of $W = a(\cos\theta + \sin\theta)$ along the y-axis. The "composition space" for this and related binary structures is a line segment, where the two extremities represent periodic crystals: at one extremity is a tiling consisting only of A-tiles, and at the other only B-tiles. In the select-and-project method, these correspond to selection stripes with the angle θ equal to 0 and $\pi/2$, respectively (namely the stripes S_2 and S_1 in Fig.27). The periodic approximants of the Fibonacci sequence are obtained by stripes with the rational slopes F_{n-1}/F_n where the F_n are the Fibonacci numbers, obeying the recursion relation $F_n = F_{n-1} + F_{n-2}$ with $F_0 = F_1 = 1$. The sequence ABABABAB, for example, is a periodic approximant of slope $F_0/F_1 = 1$ ($\theta = \pi/4$), the next approximant is the sequence ABAABAABA... and has a selection stripe of slope $F_1/F_2 = 1/2$, and so on, the lengths of the approximants increasing with n, resulting in the Fibonacci sequence when n goes to infinity.

Thanks to this 2D representation of the quasicrystal it is simple to compute the Fourier transform (FT) of the Fibonacci sequence. We will assume the spatial distribution $\rho(x) = \sum_j \delta(x - x_n)$ where x_n is the coordinate of the nth site. In the 2D representation, the mass density can be expressed as a product, as follows

$$\rho(\vec{R}) = \rho_{sl}(\vec{R})\ \chi(\vec{R})$$

$$\rho_{sl}(\vec{R}) = \sum_{m,n} \delta(\vec{R} - \vec{R}_{mn}) \tag{70}$$

where ρ_{sl} denotes the square lattice mass density, with $\vec{R}_{mn} = ma\vec{u}_X + na\vec{u}_Y$ are the vertices. The function χ takes the value 1 if $\vec{R}$ lies inside the strip, i.e if the projection $0 < \vec{R}.\vec{u}_y < W$ and 0 otherwise. It follows from the relation 70 that the FT of the sequence is given by a convolution of the FTs of the square lattice, $\rho_{sl}(\vec{Q})$ – non-zero for $\vec{Q} = \vec{G}_{h,k} = \frac{2\pi}{a}(h\vec{u}_X + k\vec{u}_Y)$ – and that of the function χ, defined by

$$\chi(\vec{Q}) = \int d\vec{R}\ e^{i\vec{Q}.\vec{R}}$$

$$\sim V\delta(q_x)\int_0^W dy e^{iq_y y}\chi(q_y) \tag{71}$$

In the second line above we have changed the integration variables in the rotated basis, where

$$q_x = \frac{2\pi}{a}(h\cos\theta + k\sin\theta)$$

$$q_y = \frac{2\pi}{a}(-h\sin\theta + k\cos\theta) \tag{72}$$

The resulting $S(q_x)$ has Bragg peaks along the q_x-axis at positions indexed by h,k. Their intensities are given by $|\chi(q_y)|^2 = \frac{4\sin^2(q_y W/2)}{q_y^2}$. The projections of the 2D reciprocal lattice points gives rise to a dense set of Bragg peaks along the q_x axis. However the intensities for most of the peaks are negligibly small, and only a subset of the peaks corresponding to small q_y values are observable (see Fig.28). For approximants, the analysis proceeds along similar lines. The principal difference arises due to the fact that the stripe has a rational slope. As a result, the Bragg peaks are spaced regularly with $\Delta q = 2\pi/L$, where L is the length of the approximant. Their intensities are given by the FT of the χ function

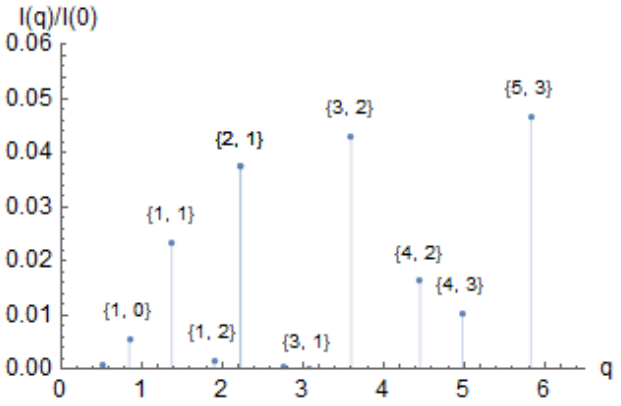

Fig. 28 Structure factor $S(q)$ plotted versus (physical space wave vector q (in units of 2π) for the perfect Fibonacci sequence. The indices above each peak indicate the corresponding 2D reciprocal lattice vector $\vec{G}_{h,k}$

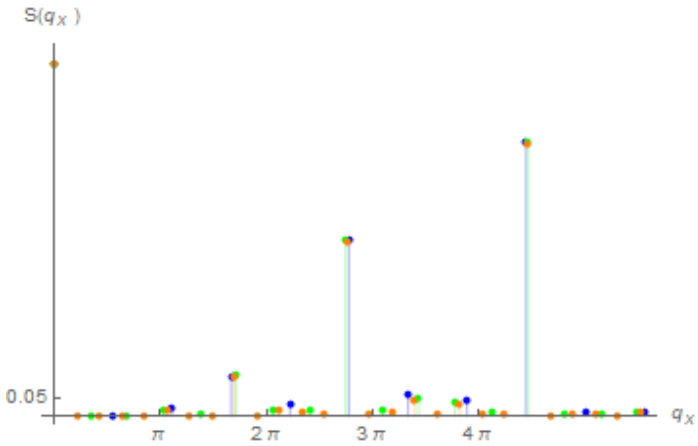

Fig. 29 Structure factors for three successive approximants of number of sites equal to 5 (blue), 8(green) and 13 (orange).

defined with respect to the appropriate selection strip. The right-hand side of Fig.28 shows the structure factors of three approximant sequences to illustrate the manner in which the structure factor of approximants approach that of the infinite quasicrystal.

E.2 Square-triangle approximant phases

We can now extend these ideas to a perfect dodecagonal quasicrystal (ie, with no disorder) using the lift construction in the 4D superspace (see section A. In that case, the lifted vertices lie within an infinite stripe whose orientation is parallel to the physical axes. Their projections onto the perpendicular space $P_\perp$ lie within a selection window W of finite extent and having a 12-fold symmetry (see Figure 14). As for the Fibonacci sequence, the mass density is a product of the 4D periodic lattice and a function χ. Thus the FT of the tiling is given by the convolution of two structure factors. The first is that of the 4D reciprocal lattice, (see section A.3), whose basis vectors project onto a star of 12 vectors in the physical plane P. These are given by[28]

$$G_n^* = \frac{2\pi}{a\sqrt{3}}(\cos\frac{(n-1)\pi}{6}, \sin\frac{(n-1)\pi}{6}) \tag{73}$$

where a is the edge length of the tiles. As was already noted in the real space description, only four of the twelve reciprocal lattice vectors G_n^* are rationally independent. They are labelled $(\boldsymbol{e}_1^*, \boldsymbol{e}_2^*, \boldsymbol{e}_3^*, \boldsymbol{e}_4^*)$ (see Figure 20 in section A.3). Thus, there are Bragg peaks at $\vec{q}_\parallel$ positions which can be indexed by the integers h,k,l,m representing linear combinations of these four reciprocal lattice vectors. The intensities of each peak depends on these indices via the FT of the window W, and again, the observable peaks correspond to perpendicular space coordinates $\vec{q}_\perp$ which are small $(aq_\perp \leq 1)$.

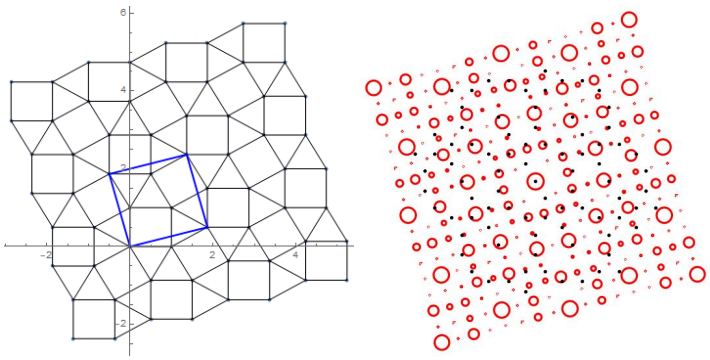

Fig. 30 (left) The sigma phase structure showing a unit cell outlined in blue. Its composition is given by $X = -0.268...$ and $Y = Z = 0$ with $\tau = 0.464....$ (right) Structure factor of the sigma phase in the (q_x, q_y) plane. Circles have radii corresponding to the peak intensity. Black dots indicate peak positions for the perfect quasicrystal showing the shifts due to finite global phason strain.

Turning next to the sigma phase shown in Fig. 30, the lift procedure yields a stripe which is inclined with respect to the plane P. This is encoded by the global phason strain B (see section 5.2). For this periodic approximant, the stripe has a rational direction in the 4D superspace. One can once again define a selection window by a region W in the plane perpendicular to the strip. As seen before for the approximants of the quasicrystal, the peaks in the reciprocal space $\vec{q}_\parallel$ lie on a grid of spacing $2\pi/L$ where L is the period of the crystal. Fig.30 shows the structure factor – the radius of the red circles is proportional to the intensity of the peak. We note that these peaks are shifted with respect to the positions quasicrystal (shown by black dots) because the projection axes are slightly rotated with respect to the perfect QC.

A similar argument applies in the case of a bigger square approximant phase, of larger periodic length L based on repeating dodecagonal wheels as illustrated in Fig. 31. The structure factor of this phase is shown superimposed upon that of the sigma phase, showing the small shifts that occur when going from one approximant to the next. In the limit of the stripe becoming horizontal, one converges to the structure factor of the perfect quasicrystal.

Several comments are now in order. 1) in contrast to the Fibonacci sequence the window W has a fractal structure for the square triangle dodecagonal QC. As a result, Bragg peaks scale as a fractional power in the system size rather than linearly. It would however be probably very difficult to experimentally measure this type of scaling. 2) The discussion given above can be

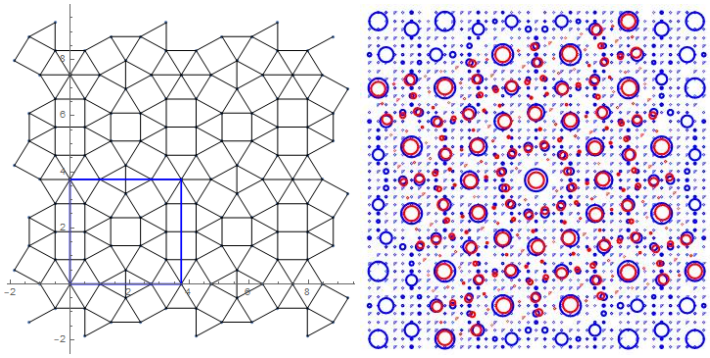

Fig. 31 (left) A periodic square approximant phase with the unit cell outlined in blue. Its composition is given by $X = 0.1436...$ and $Y = Z = 0$ with $\tau = 0.4897....$ (right) The structure factor shown by blue circles. At each peak position the circle size is proportional to the intensity.

extended to random tilings, for which the selection stripe has an irregular “wavy" form in 4D. The analysis in this case predicts a structure factor with broadened peaks of diminished intensity due to a disorder-induced Debye-Waller type factor, and in addition a diffuse background.[28]